Journal of Controlled Release 385 (2025) 113978

Contents lists available at ScienceDirect

Journal of Controlled Release

journal homepage: www.elsevier.com/locate/jconrel

In situ construction of ossification micro-units for critical bone regeneration *via* sustained lifting of epigenetic suppression

Wu Yang [a,b,c,1], Tao Ding [b,1], Pengzhen Zhuang [a,b,c,1], Yu Chen [a,b,c], Yu Zhang [a,b,c], Zehao Chen [b], Minjie Fan [a,b,c], Tapani Viitala [c,e], Zhongmin Wang [a], Wenguo Cui [b,**], Hongbo Zhang [a,b,c,d,*]

[a] Department of Radiology, Ruijin Hospital Lu Wan Branch, Shanghai Jiaotong University School of Medicine, Shanghai 200025, P.R. China
[b] Department of Orthopaedics, Shanghai Key Laboratory for Prevention and Treatment of Bone and Joint Diseases, Shanghai Institute of Traumatology and Orthopaedics, Ruijin Hospital, Shanghai Jiao Tong University School of Medicine, 197 Ruijin 2nd Road, Shanghai 200025, PR China
[c] Pharmaceutical Sciences Laboratory, Faculty of Science and Engineering, Åbo Akademi University, Turku 20520, Finland
[d] Turku Bioscience Centre, University of Turku and Åbo Akademi University, Turku 20520, Finland
[e] Drug Research Program, Division of Pharmaceutical Chemistry and Technology, Faculty of Pharmacy, University of Helsinki, 00014 Helsinki, Finland

ARTICLE INFO

Keywords:
Microgel
Intramembranous ossification
Calcium phosphate nanoparticles
Epigenetic suppression
Bone regeneration
siRNA

ABSTRACT

Critical-sized bone defects present significant clinical challenges due to insufficient stem cell recruitment, epigenetic suppression of osteogenesis, and inadequate mineralization. Among the epigenetic suppression mechanisms, upregulated MEG3 specifically recruits the epigenetic regulator EZH2 to block the transcription of β-catenin, a core gene for bone regeneration. To regulate MEG3 *in vivo* effectively, we used microfluidics to develop *in situ* continuous MEG3-silencing ossification micro-units (MSOMs) that integrate "material–gene–biofactor" tri-coupling into a unified biomaterial system. The MSOMs are nano-micro particles composed of amorphous calcium phosphate nanoparticles loaded with siRNA (si@BCP) in GelMA microgels loaded with stromal cell-derived factor-1α (SDF-1α). The SDF-1α in the microgel layer is rapidly released to recruit BMSCs, while the siRNA in si@BCP has sustained release to silence MEG3 and restore β-catenin transcription continuously. Thus, the MSOMs provide a stable mineralization microenvironment for ossification center formation. *In vivo* observations revealed the formation of ossification centers around these micro-units, tripling new bone formation and achieving efficient bone regeneration. By addressing the key limitations of traditional therapies, MSOMs offer a clinically viable solution that integrates stem cell recruitment, epigenetic regulation, and biomaterial-based mineralization, thus providing a highly efficient approach for critical bone defect repair.

1. Introduction

With the increasing incidence of critical bone defects in clinical settings, orthopedic treatments face the formidable challenge of achieving effective and reliable bone regeneration within the shortest possible timeframe [1,2]. Traditional therapeutic approaches, such as autologous or allogenic bone grafts and synthetic bone substitutes, often encounter limitations due to donor site scarcity, immune rejection, and biocompatibility issues, struggling to meet clinical demands [3–5]. Regeneration of critical bone defects primarily hinges on intramembranous ossification—a process where bone marrow stem cells (BMSCs) are recruited, differentiate into osteoblasts, and form new bone [6,7]. This process accelerates tissue development and enhances repair success rates. However, the success of this process crucially depends on the efficient recruitment, osteogenic differentiation (OGD), and mineralization of BMSCs [8,9]. Critical bone defects often lack adequate

* Corresponding author at: Department of Radiology, Ruijin Hospital Lu Wan Branch, Shanghai Jiaotong University School of Medicine, Shanghai 200025, P.R. China.
** Corresponding author at: Department of Orthopaedics, Shanghai Key Laboratory for Prevention and Treatment of Bone and Joint Diseases, Shanghai Institute of Traumatology and Orthopaedics, Ruijin Hospital, Shanghai Jiao Tong University School of Medicine, Shanghai 200025, P. R. China.
E-mail addresses: wgcui@sjtu.edu.cn (W. Cui), hongbo.zhang@abo.fi (H. Zhang).
[1] These authors contributed equally to this work.

https://doi.org/10.1016/j.jconrel.2025.113978
Received 17 May 2025; Received in revised form 9 June 2025; Accepted 21 June 2025
Available online 23 June 2025

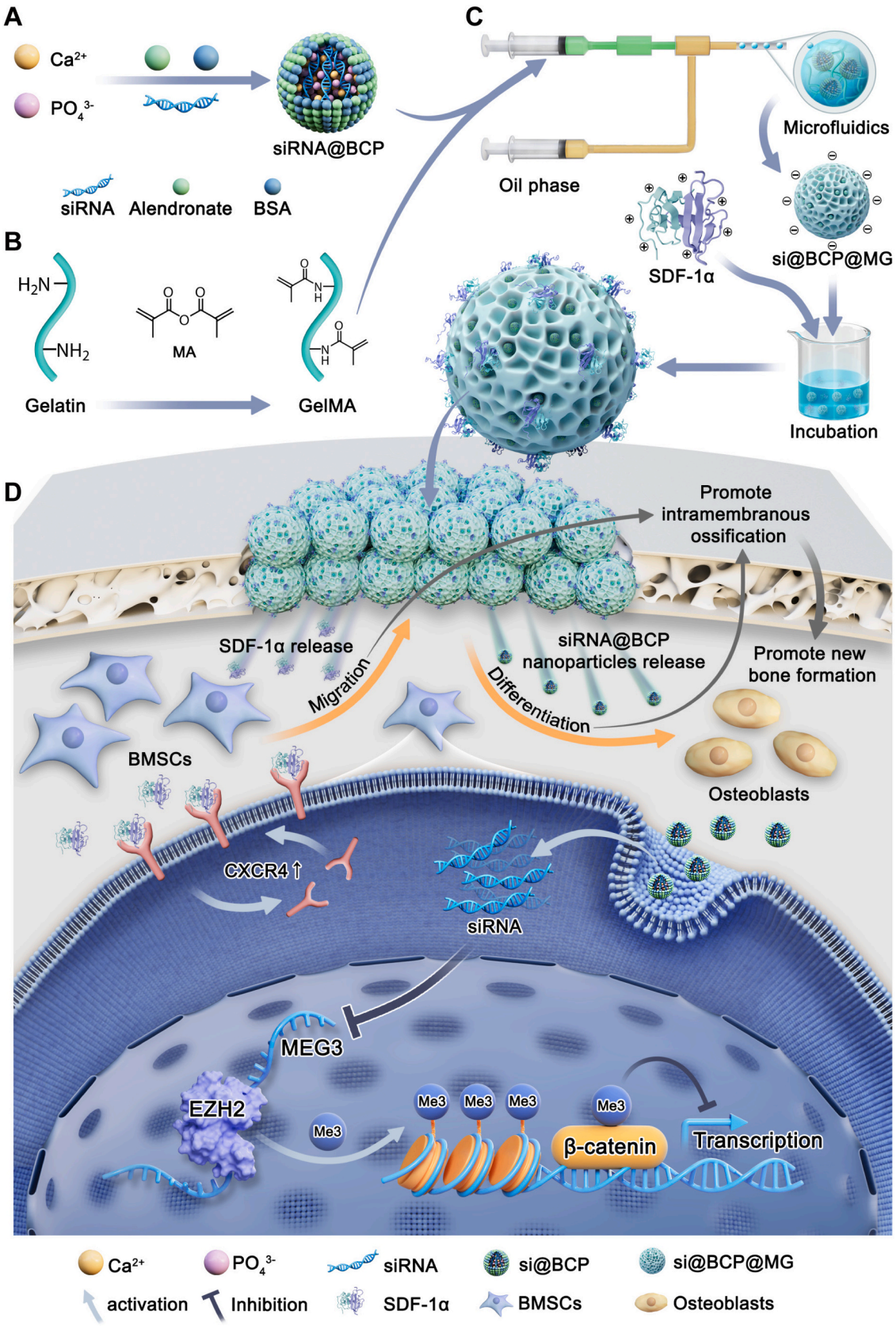

Scheme 1. Construction and mechanism of action of the *in situ* continuous MEG3-silencing osteogenic micro-units (MSOMs). (A) Preparation of si@BCP nanoparticles. (B) Fabrication of GelMA. (C) MSOMs fabrication based on microfluidics, comprising physically encapsulated si@BCP and electrostatically adsorbed SDF-1α. (D). Mechanism of action of MSOMs in promoting the repair of critical bone defects. Specifically, MSOMs facilitate the rapid release of SDF-1α to attract BMSCs. Additionally, the continuous internalization of si@BCP nanoparticles by BMSCs allows for the release of siRNA to silence MEG3, disrupt the recruitment of EZH2, lift epigenetic suppression of β-catenin, and promote BMSC-mediated intramembranous ossification and new bone formation.

chemotactic signals, impeding BMSC migration to defect sites and resulting in a severe shortage of cellular resources [10,11]. Additionally, epigenetic modifications often suppress OGD by downregulating osteogenesis-related genes without altering the DNA sequence, thereby hindering mineralization and subsequent new bone growth [12–14]. These issues prevent effective bone formation through intramembranous ossification, leading to failed bone repair, and challenge traditional methods that are ineffective at reversing epigenetic suppression. Such difficulties underscore the urgent need for innovative integrated strategies that not only enhance BMSC recruitment but also effectively counteract epigenetic suppression and improve mineralization, thereby optimizing the healing of critical bone defects.

Recent advances in epigenetic modification have shown promise in promoting bone regeneration through targeted interventions in DNA methylation and non-coding RNA regulation [15–17]. Despite some success in facilitating fracture healing and intramembranous ossification [18,19], challenges persist in achieving precise, effective, and continuous epigenetic regulation *in vivo*. Notably, lncRNA maternally expressed gene 3 (MEG3), a crucial player in epigenetic mechanisms located at chromosome 14q32.3, has crucial regulatory functions in bone tissue [20]. Studies indicate that MEG3 is upregulated in non-healing fracture tissues and downregulated during OGD [21,22]. Furthermore, upregulated MEG3 mediates epigenetic suppression by specifically binding and recruiting the epigenetic regulator enhancer of zeste homolog 2 (EZH2) to the promoter region of the core bone regeneration gene β-catenin, silencing β-catenin and inhibiting OGD [23]. Therefore, a strategy centered on silencing MEG3 could effectively remove the epigenetic blocks on β-catenin, reactivating osteogenesis-related gene expression and significantly enhancing bone healing. However, the technical challenge lies in consistently achieving this epigenetic regulation within the bone tissue environment, particularly in bridging the gap between cellular and tissue dimensions to ensure the integration of these micro-level interventions into the macro-systems suitable for bone regeneration.

Addressing the challenge of bridging microscale genetic strategies with macroscale clinical applications is essential due to the size disparity between cellular behaviors and tissue-scale requirements, necessitating the development of micro-nano structures that align cellular actions with tissue demands and foster a suitable environment for BMSCs in defect areas [24]. Here, we have developed a novel *in situ* continuous MEG3-silencing ossification micro-units (MSOMs), which integrates 'material-genetic-biofactor' tri-coupling into a cohesive strategy (Scheme 1). Specifically, MEG3-targeting small interfering RNA (siRNA), bovine serum albumin (BSA), and alendronate (ALN) are co-precipitated with calcium phosphate (CaP) to produce siRNA-loading and dispersible and stable BCP (si@BCP) nanoparticles [25,26]. While Amorphous CaP possesses excellent bioactivity, it is intrinsically unstable and prone to aggregation due to its high surface energy. The incorporation of BSA and ALN during synthesis effectively mitigates these drawbacks, resulting in structurally stable and uniformly dispersed nanoparticles. Subsequently, gelatin methacryloyl (GelMA) microgels are formed using microfluidic technology by which si@BCP nanoparticles and stromal cell-derived factor-1α (SDF-1α) are sequentially loaded into microgels to form the MSOMs. The MSOMs integrate critical strategies for BMSC recruitment, epigenetic modification, and the enhancement of the mineralization microenvironment, thereby improving the potential for effective repair of critical bone defects.

2. Methodology

2.1. Reagents

Unless otherwise specified, all chemical reagents were purchased from Sigma-Alrich, Macklin Co., Sangon Biotech, or Aladdin.

2.2. Synthesis and characterization of BCP nanoparticles

Following earlier methods [27], solutions I and II were prepared to synthesize CaP. All the chemicals were dissolved in DEPC-treated water. Solution I contained 2 mL of DEPC-treated water, 0.42 mL of $CaCl_2$ solution (2 M), and 0.84 mL of Tris-HCl solution (10 mM, pH = 10). Solution II consisted of 0.3 mL DEPC-treated water and 0.43 mL HEPES buffer (containing 280 mM NaCl, 15 mM Na_2HPO_4, and 50 mM HEPES). Following careful mixing, Solution II was gradually added to Solution I while being stirred at 500 rpm, and the mixture was continuously stirred for an additional 30 min. For BCP synthesis, following the mixing of Solutions I and II, ALN (1 mg/mL) and BSA (5 mg/mL) were added sequentially and then stirred for 30 min. If siRNA or Cy3-siRNA was loaded, siRNA was pre-mixed in Solution I and incubated for 5 min. Post-stirring, the mixture was centrifuged at 12,000 *g* for 10 min, and siRNA loading efficiency was measured. After washing the nanoparticles three times, they were dispersed in DEPC-treated water at 1 mg/mL for storage. Nanoparticles diluted to 0.1 mg/mL in DEPC-treated water were observed under a transmission electron microscope (TEM) to determine the particle size and shape, dynamic light scattering (DLS) was used to measure Zeta potential, and FTIR was employed to detect functional groups.

2.3. Loading and encapsulation of siRNA in CaP and BCP nanoparticles

The experimental steps were slightly modified from previous methods [27]. Various mass ratios (1:5, 1:10, 1:15, 1:20) of siRNA were pre-mixed with Solution I to synthesize si@BCP. Free siRNA was detected using a Nanodrop 1000c, and loading efficiency was calculated. 1 % agarose gel electrophoresis was used to assess encapsulation effectiveness. After dilution, samples were mixed with 6 × loading buffer and electrophoresed at 80 V for 30 min, and siRNA bands were observed using a gel imaging system.

2.4. Preparation and physical characterization of MSOM

GelMA synthesis was performed similarly to previous methods [28]. Specifically, 200 mL of carbonate buffer (pH = 9.0) was used to dissolve 20 g of Type B gelatin, and the liquid was stirred at 40 °C until it formed a uniform amber liquid. The reaction lasted three hours after methacrylic anhydride (MA) was introduced to the gelatin solution at 0.2 mL/min. After adding 100 mL of PBS (pH = 7) to stop the reaction, the unreacted gelatin was removed by centrifugation at 8000 rpm for 15 min. After being moved into an 8000 KDa dialysis bag, the supernatant was dialyzed for two days at 40 °C, with MQ water being changed four times daily. Post-dialysis, impurities were removed using a 0.22 μm filter, and the product was lyophilized and stored in the dark at −20 °C.

GelMA microgels were prepared as previously described [29]. A 5 % (*w/v*) GelMA solution was prepared, adding 0.5 % (w/v) photoinitiator lithium phenyl-2,4,6-trimethylbenzoylphosphinate (LAP). To fabricate siNC@BCP@MG and si@BCP@MG, 1 mg/mL siNC@BCP nanoparticles or si@BCP nanoparticles were added, respectively. Using a microfluidic device, the inner phase consisted of GelMA solution (with or without siNC@BCP nanoparticles or si@BCP nanoparticles), and the outer phase was liquid paraffin containing 5 % Span 80. The formed microdroplets were frozen at −80 °C for 30 min, then cross-linked under 405 nm UV light for 5 min. Liquid paraffin was removed using anhydrous ether, followed by six washes with MQ water. The microgels were lyophilized, sterilized under UV overnight, and stored at −20 °C. Microgel morphology and size distribution were observed using an inverted fluorescent microscope. Scanning electron microscopy (SEM) was used to observe the pore size and morphology of the lyophilized microgels.

2.5. Swelling of MG and si@BCP@MG

The swelling experiment was slightly modified from previous reports

[30]. To replicate physiological conditions, 10 mg of si@BCP@MG and freeze-dried MG were put in 1 mL of PBS and shaken at 37 °C. Excess liquid was removed at 0.5, 1, 2, 3, and 4 h, and the swollen microgel weight ($W_{swollen}$) was recorded. Swelling ratio (Q) was calculated as follows:

$$Q\ (\%) = \frac{(W_{swollen} - W_{tube})}{(W_{dry} - W_{tube})} \times 100\% \quad (1)$$

where $W_{swollen}$ is the weight of the swollen microgel tube, W_{dry} is the weight of the dry microgel tube, and W_{tube} is the weight of the empty tube. The swelling ratio was calculated and plotted against time to analyze the swelling kinetics.

2.6. Fabrication of MSOM

To fabricate MSOM, 10 mg of si@BCP@MG was placed in a solution containing 1 mL of SDF-1α (300 ng/mL) and incubated overnight on a shaker at 4 °C. Then, the supernatant was gathered, and the loading rate was determined by measuring the amount of unbound SDF-1α using an Enzyme-linked immunosorbent assay (ELISA). The loading efficiency of SDF-1α on the microgels was calculated using the following formula:

$$\text{Loading efficiency}\ (\%) = \frac{W_{Initial} - W_{Unbound}}{W_{Initial}} \times 100\% \quad (2)$$

where $W_{Initial}$ is the initial mass of SDF-1α, and $W_{Unbound}$ is the mass of unbound SDF-1α.

2.7. Degradation of MG and MSOM

The degradation of MG and MSOM was slightly modified from previous reports [30]. Briefly, 1 mL of sterile PBS containing collagenase II (100 μg/mL) was mixed with 15 mg of sterilized, lyophilized microgels and shaken at 37 °C. Samples were collected at different times, centrifuged to remove the supernatant, and washed three times with MQ water. The remaining microgel weight was then lyophilized and recorded. The degradation rate was calculated as follows:

$$\text{Degradation rate}\ (\%) = \left[1 - \frac{W_{\text{remaining}} - W_{\text{tube}})}{(W_{\text{initial}} - W_{\text{tube}})}\right] \times 100\% \quad (3)$$

where $W_{remaining}$ is the remaining dry weight of the microgel with EP tube, $W_{initial}$ is the initial dry weight of the microgel with EP tube, and W_{tube} is the weight of the empty EP tube.

2.8. Release of SDF-1α from MSOM

Transferring 10 mg of SDF-1α-loaded MSOM to 1 mL of sterile PBS, the mixture was shaken at 37 °C to imitate release. Samples were collected on different days. The same volume of sterile PBS was used to replace the 200 μL of supernatant that was removed. The samples were kept at −80 °C, and SDF-1α concentration was detected using ELISA. The cumulative SDF-1α release was calculated using the formula:

$$Q_t = C_t \times V + \sum_{i=1}^{t-1} (C_i \times V_{sample}) \quad (4)$$

where Q_t represents the cumulative release of SDF-1α at time t, C_t represents the apparent concentration of SDF-1α at time t, V represents the total volume of the release medium, V_{sample} represents the volume of the sample taken, C_i represents the concentration of SDF-1α at the previous time point.

2.9. Release of si@BCP nanoparticles from MSOM

Cy3-labeled siRNA was used to prepare MSOM. After adding 15 mg of freeze-dried MSOM to 1 mL of sterile PBS mentioned in *2.7*, the mixture was shaken at 37 °C. At various times, 200 μL of liquid was taken, and the same volume of new enzyme solution was added. A fluorescence plate reader was used to detect the absorbance, and the formula was used to determine the cumulative release rate:

$$Q_t = \sum \left(C_t \times V + \sum C_i \times V_{\text{sample}}\right) \quad (5)$$

where Q_t represents the cumulative release of si@BCP at time t, C_t represents the concentration of si@BCP at time t, V represents the total volume of the release medium, V_{sample} represents the volume of the sample taken, C_i represents the concentration of si@BCP at a previous time point.

2.10. Cell culture and transfection

Rat BMSCs were acquired from Cyagen (Suzhou, China) and cultivated in an incubator set at 37 °C with 5 % CO_2 in α-MEM with 10 % FBS, 100 U/mL penicillin, and 100 mg/mL streptomycin. Cy3-labeled siRNA was used to prepare si@CaP and si@BCP nanoparticles for transfection. BMSCs were seeded and transfected at 70–80 % confluence with siRNA, si@CaP nanoparticles, and si@BCP nanoparticles resuspended in Opti-MEM at a concentration of 100 nM siRNA. After 6 h, transfection efficiency was assessed by flow cytometry, and cells were observed and photographed.

2.11. CCK-8 assay and Calcein-AM/PI staining

BMSCs were seeded in a 96-well plate and adhered before adding sterilized microgels. Cells were washed three times at various time points and incubated with CCK-8 solution (Complete medium:CCK-8 solution = 9:1) in the incubator for one hour. A BioRad microreader was used to detect absorbance at 450 nm. For Calcein-AM/PI staining, cells were gently washed and treated with Calcein-AM/PI staining solution (Beyotime, China), and incubated at 37 °C for 30 min. Cells were observed and photographed.

2.12. Migration assay

Scratch and Transwell assays were used to measure the migration of BMSCs. BMSCs were seeded at 5×10^5 cells per well for the scratch assay in 6-well plates. A 200 μL pipette tip was used to make a scratch once 100 % confluence was achieved. PBS was used to wash the cells before Calcein-AM/PI staining was applied for imaging. Following the addition of 2 mL of α-MEM containing 2 % FBS, microgels were put in a Transwell insert (0.4 μm, NEST) for co-cultivation. Cells were cleaned and stained at different intervals, and Image J was used to determine the wound-healing percentage. The Transwell assay was conducted similarly to previous reports [24], with 200 μL BMSCs (2×10^4 cells) being seeded in the a Transwell insert (8 μm, NEST), while the lower chamber had 600 μL of media containing microgels. After 24 h, cells were fixed and stained with 0.1 % crystal violet. The migrated cells were observed, photographed, and quantified using Image J software.

2.13. In vitro capture of BMSCs by MSOM

This assay was slightly modified from previous reports [30]. Briefly, a 2 mL EP tube holding about 200 microgels received 1 mL of the reconstituted BMSC suspension (1×10^4 cells). These tubes were incubated at 37 °C, 5 % CO_2, and gently rotated every 30 min to ensure even distribution. After 6 and 12 h, microgels were gently washed to get rid of uncaptured cells. BMSCs were stained and observed. Furthermore, after 12 h of co-culture, uncaptured BMSCs were washed away with PBS, and microgels with captured BMSCs were dispersed in a complete medium, seeded onto 12-well plates, and cultured for three additional days before staining and imaging again. The cells were calculated using Image J software.

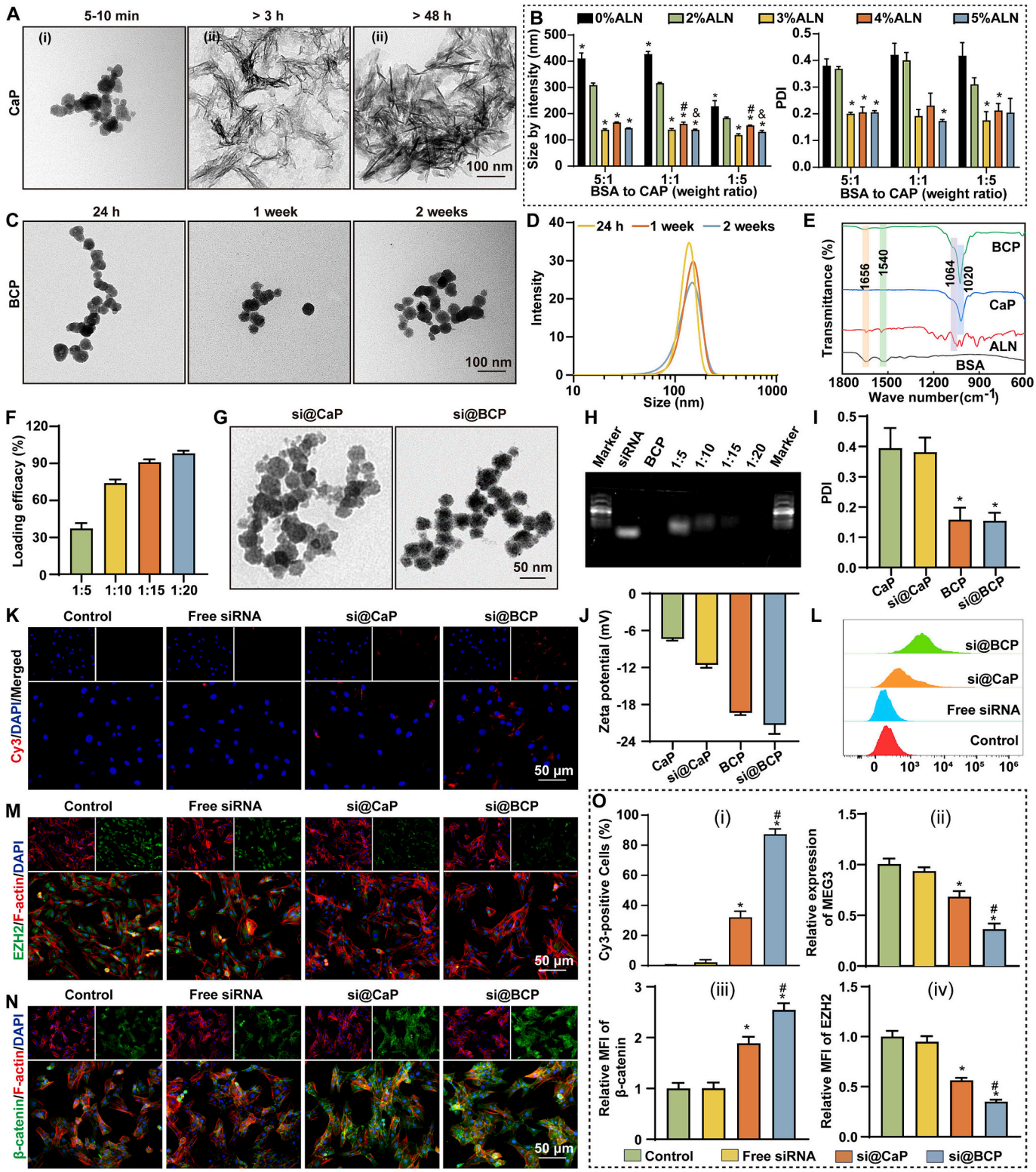

Fig. 1. Optimization of BCP nanoparticle synthesis, siRNA loading, and transfection. (A) TEM images of CaP nanoparticles (NPs) stored in an aqueous solution at different times. (B) Average size and PDI of CaP NPs with different ALN and BSA incorporation ratios (All $n = 3$; * indicates $p < 0.05$, in comparison with 2 % ALN; # indicates $p < 0.05$, in comparison with 3 % ALN; & indicates $p < 0.05$, in comparison with 4 % ALN). (C) TEM images of BCP NPs. (D) Size distribution of BCP NPs. (E) FTIR spectra. (F) Loading of siRNA to BCP NPs with different weight ratios (n = 3). (G) TEM images of si@CaP and si@BCP NPs. (H) Agarose gel electrophoresis was used to detect free siRNA after loading BCP NPs with siRNA at different mass ratios. (I) PDI of CaP, si@CAP, BCP, and si@BCP NPs (n = 3). (J) Zeta potential data of CaP, si@CAP, BCP, and si@BCP NPs (n = 3). (K) Cellular uptake of free siRNA, si@CaP, and si@BCP NPs by BMSCs. (L) Flow cytometry for detecting uptake of free siRNA, si@CaP, and si@BCP NPs by BMSCs. (M) and (N) IF staining of EZH2 (M) and β-catenin (N) in BMSCs. (O) (i) Quantitative analysis of Cy3-positive cells in flowcytometry; (ii) RT-qPCR showed relative expression of MEG3 in BMSCs; (iii) and (iv) semi-quantitative analysis for IF staining of EZH2 (iii) and β-catenin (iv) (All n = 3; $p < 0.05$ was indicated by the symbols * and # when compared to the Control and si@CaP groups, respectively).

2.14. Induction of OGD and staining

BMSCs were seeded in 24-well plates and then cultivated in a complete medium for the entire night. OGD medium (containing 10 % FBS, 100 nM dexamethasone, 10 mM β-glycerophosphate, 50 μg/mL L-ascorbic acid, 100 U/mL penicillin, and 100 mg/mL streptomycin) was added after MSOM adding to the upper chamber of a Transwell system the following day, with the medium being changed every three days. Following seven days of OGD, the media was taken out, the cells were washed, and they were fixed for half an hour with 4 % paraformaldehyde (PFA) in preparation for ALP staining. Following several PBS washes, cells were stained for half an hour at room temperature (RT) in the dark with NBT/BCIP solution. Gross and microscopic images of ALP staining were captured, and the percentage of ALP-positive staining was analyzed using Image J software. For ARS staining, on day 14 of OGD, after removing the medium, the cells underwent PBS washes, fixation, and washing. After adding the ARS staining solution, the samples were put at RT for ten minutes before the stain was removed and then washed three times with MQ water. Gross photographs and microscopic images of the mineralized nodules were then taken. A microplate reader was used to measure the absorbance at 562 nm after the stained sample was dissolved in 10 % cetylpyridinium chloride and left in the dark for 30 min in order to examine ARS staining quantitatively.

2.15. Real-time quantitative PCR (RT-qPCR)

After collecting BMSCs at different intervals after transfection or microgel co-cultivation, the RNA was extracted using a Simply P Total RNA Extraction Kit (Bioflux, China) and dissolved in water treated with DEPC. Samples were kept at −80 °C, and the RNA concentration was determined. A PrimeScript RT Reagent Kit (Takara, Japan) was utilized to reverse-transcribe RNA to cDNA. qPCR was performed using a TB Green Pre-mix Ex Taq II Kit (Takara, Japan) on an ABI 7500 system (ABI 7500, Thermo Fisher Scientific, Inc. USA) with cycling conditions of 95 °C for 5 min, followed by 40 cycles of 95 °C for 10 s and 60 °C for 30 s. The $^{\Delta\Delta}$Ct technique was used to calculate relative gene expression, with GAPDH as an inner reference gene. SangonBiotech generated all the primers, and Supplementary Table 1 contains the sequences.

2.16. Immunofluorescence (IF) staining

BMSCs were treated as mentioned in *2.14*. Following co-cultivation, cells underwent a PBS wash, a 4 % PFA fixation, a 10-min permeabilization with 0.1 % Triton X-100, and an hour-long block. Primary antibodies against CXCR4 (Affinity, China), EZH2 (Proteintech, USA), β-catenin (Proteintech, USA), Collagen I (Col I, Affinity, China), and Osteopontin (OPN, Proteintech, USA) (all dilution ratio 1:200) were added and incubated incubated at 4 °C for the entire night. Following washes, secondary antibodies labeled by Alexa Fluor 488 (Affinity, China, 1:200) were added and incubated for 1 h at RT, followed by Alexa Fluor 555-conjugated Actin Tracker (Beyotime, 1:400) for 30 min. Nuclei was then dyed by 4′,6-diamidino-2-phenylin-dole (DAPI, Beyotime), and fluorescence images were captured in three random fields per sample, with MFI quantified using Image J.

2.17. Animal study and ethics

This study's animal experiments were approved by the Institutional Animal Care and Use Committee (IACUC) of Shanghai Shengchang Biotechnology Co., Ltd. (Approval No: 2022–06-RJYY-YW-108) and conducted according to the PREPARE guidelines reported by Smith [31]. Thirty-two male Sprague-Dawley (SD) rats (250–300 g) were used. Different microgels were injected under the periosteum of the skulls of twelve rats to assess *in vivo* recruitment of BMSCs. Twelve rats were anesthetized with isoflurane, followed by skin preparation and disinfection. A scalp incision was performed longitudinally, the periosteum was gently separated, sterile microgels were injected subperiosteally, and the skin was sutured. After 7 days, rats were euthanized with an overdose of isoflurane, and the tissue areas containing the microgels were excised, fixed, embedded, and prepared for sectioning. Hematoxylin and eosin (H&E) staining and Masson trichrome staining were conducted to evaluate tissue architecture. Immunohistochemistry (IHC) staining was used to examine CD44, CD90, β-Catenin, and OPN expression, with positive cells quantified using Image J software.

Five groups of twenty rats, each consisting of four rats, were performed. After anesthesia with isoflurane, the rats were prepped and disinfected. A trephine drill was used to produce a cranial defect with a diameter of 5 mm, microgels were implanted, and the wound was sutured. After 8 weeks, the rats were euthanized by inhalation of an overdose of isoflurane, and cranial samples were collected. High-resolution micro-CT was used to scan the cranial defect samples, reconstruct 3D images, and measure bone volume (BV), total volume (TV), trabecular number (Tb.N), and trabecular thickness (Tb.Th). The cranial samples were stained after decalcification, embedding, and sectioning to evaluate tissue architecture and new bone formation. IHC staining was used to evaluate β-Catenin, OPN, and Col I expression, with the results quantitatively analyzed using Image J software.

2.18. Statistical analysis

Statistical analyses and graphical representations were used to perform using GraphPad Prism 8.0 and Origin software. Every experiment was conducted three times, and the results were displayed as mean ± standard deviation. When comparing two groups, the Student's *t*-test was utilized, and when comparing three or more groups, the one-way analysis of variance (ANOVA) was utilized. Statistical significance was defined as a *p*-value of less than 0.05.

3. Results and discussion

3.1. Optimization and characterization of ALN and BSA-modified CaP (BCP) nanoparticles

Amorphous CaP nanoparticles are promising candidates for gene delivery and have a strong capability to induce bone regeneration [32]. However, their inherent propensity to aggregate significantly restricts their uptake and transfection efficiency in cells [33]. Moreover, our previous studies demonstrated that amorphous CaP acts as a metastable precursor that rapidly transforms into hydroxyapatite in aqueous environments [34]. This transition increases particle size, which hinders cellular internalization and limits the release of loaded nucleic acids. In this work, we detected this transformation with TEM analysis. As shown in Fig. 1A, freshly prepared CaP nanoparticles exhibited a spherical morphology with uneven sizes and evident aggregation. After 3 h of dispersion in water, the amorphous CaP transitioned into larger sheet-like structures. By 48 h, the nanoparticles transformed further into clustered needle-like morphologies with significantly increased sizes, consistent with our previous findings [34]. TEM images also showed that unmodified CaP nanoparticles loaded with siRNA (si@CaP) displayed irregular shapes with significant aggregation (Fig. 1G). Similarly, the DLS results demonstrated that the unmodified CaP and si@CaP nanoparticles showed a high aggregation, with a polydispersity index (PDI) of 0.395 and 0.381, respectively (Fig. 1I). These results indicate that unmodified amorphous CaP nanoparticles are suboptimal for direct use in nucleic acid delivery and require further stabilization.

To address this limitation, we hypothesized that BSA could improve nanoparticle dispersibility, while ALN, through calcium ion chelation, could inhibit crystallization and enhance hydration stability. Accordingly, we co-introduced ALN and BSA into the precursor solution and performed formulation optimization. DLS results confirmed our hypothesis: BCP nanoparticles exhibited improved dispersibility, reduced

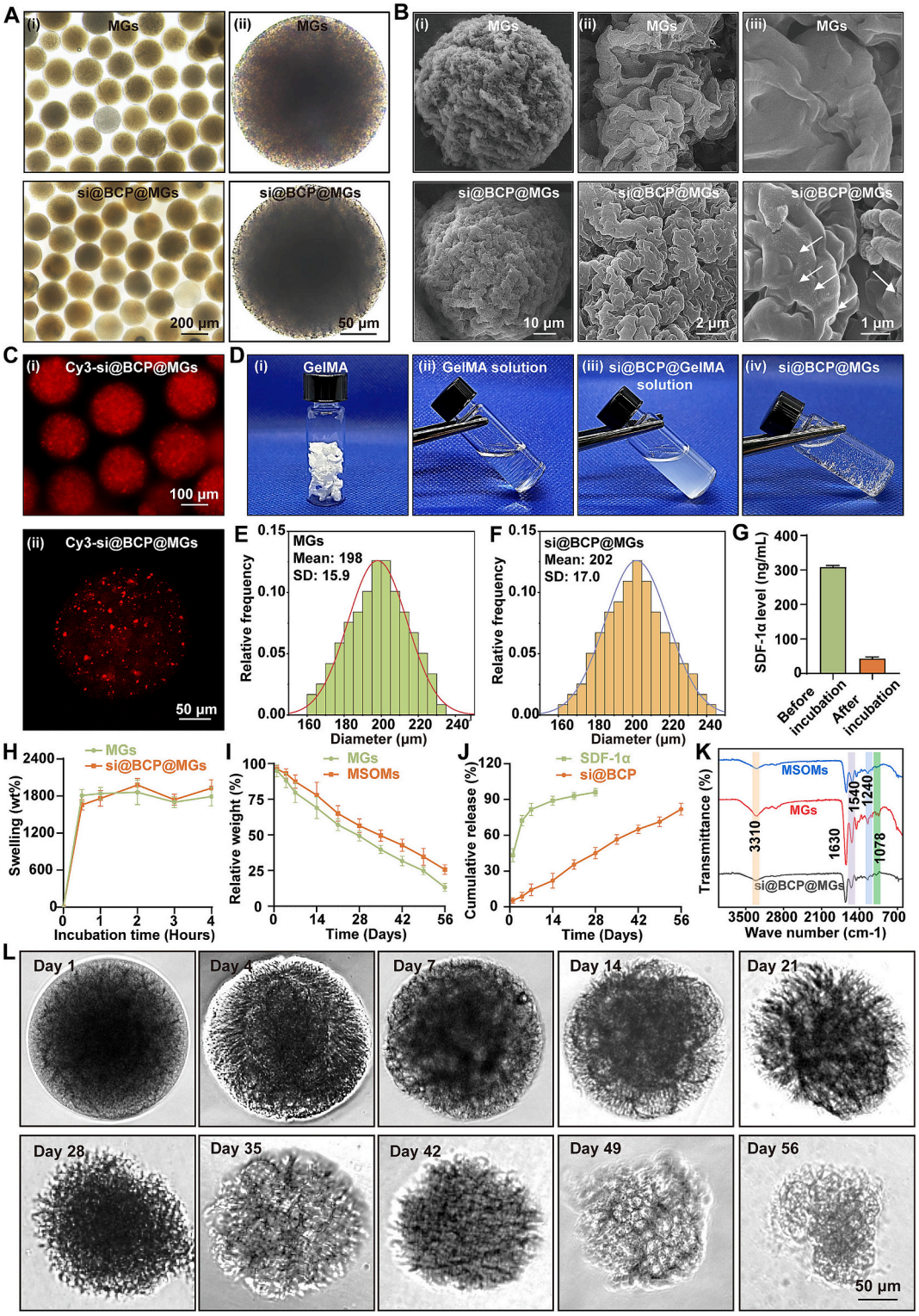

Fig. 2. Fabrication and characterization of the MSOMs. (A) Bright-field images of MGs and si@BCP@MGs (i, MGs; ii, si@BCP@MGs). (B) SEM image of MGs and si@BCP@MGs. (C) Fluorescent images and Cy3-si@BCP@MGs. (D) Flowchart of si@BCP@MGs fabrication. (E, F) Size distributions of MGs (E) and si@BCP@MGs (F). (G) SDF-1α concentration before and after incubation with si@BCP@MGs. (H) Swelling curves of MGs and si@BCP@MGs. (I) Degradation curves of MGs and MSOMs. (J) Release of SDF-1α and Cy3-si@BCP from MSOMs. (K) FTIR spectra of MGs, si@BCP@MGs, and MSOMs. (L) Morphology evolution of MSOMs over time in a collagenase II solution. All $n = 3$.

particle size, and lower PDI than unmodified CaP (Fig. 1B). Moreover, varying the ratios of ALN and BSA affected the hydrodynamic diameter and PDI of the nanoparticles. The optimal mass ratios were determined to be 3 % ALN and 20 % BSA, yielding the smallest particle size and the lowest PDI among tested formulations (Fig. 1B). TEM analysis further validated the structural stability of the optimized BCP nanoparticles. As shown in Fig. 1C, BCP exhibited a more uniform size and morphology than unmodified CaP and maintained its structure over 2 weeks. DLS

measurements also revealed minimal changes in hydrodynamic size after dispersion in water for 24 h, 1 week, and 2 weeks, with mean diameters of 137.3 nm, 149.6 nm, and 145.4 nm, respectively (Fig. 1D). These results indicate that ALN and BSA co-modification effectively stabilized BCP nanoparticles by reducing aggregation and suppressing the amorphous-to-crystalline phase transition, enhancing their suitability as gene delivery carriers.

Zeta potential and Fourier transform infrared spectra (FTIR) measurements confirmed the successful modification of the nanoparticles. Initially, the zeta potential of CaP nanoparticles was approximately −7.4 mV (Fig. 1J). The introduction of ALN and BSA altered the zeta potential of BCP nanoparticles to −19.4 mV (Fig. 1J). Additionally, FTIR spectra of BCP nanoparticles revealed the characteristic phosphate (PO_4^{3-}) peak of CaP at 1020 cm^{-1} [27], the corresponding peaks for ALN (1064 cm^{-1}) [35], and the amide I and II bands of BSA (at 1656 cm^{-1} and 1540 cm^{-1}, respectively) [36] (Fig. 1E). These results confirmed the integration of ALN and BSA into the BCP nanoparticles. Further evaluation of the biocompatibility of CaP and BCP nanoparticles showed low cytotoxicity in BMSCs, even at high concentrations (up to 100 μg/mL), indicating their suitability for *in vitro* applications and potential for *in vivo* use (Fig. S1). These findings underscore the significant improvement in dispersibility and stability achieved through the co-modification of BCP nanoparticles with ALN and BSA, thus resolving the primary limitations of unmodified CaP nanoparticles.

3.2. Optimization and transfection of siRNA with BCP in BMSCs

3.2.1. Optimization of siRNA loading efficiency

Efficient loading of siRNA onto a nanoparticle-based delivery system is a critical prerequisite for its performance in gene therapy [37]. This study selected mass ratios of 5:1, 10:1, 15:1, and 20:1 for siRNA encapsulation by utilizing agarose gel electrophoresis and ultraviolet (UV) absorption detection (nanodrop 1000c) to determine the optimal ratio for BCP loading of siRNA. The results indicated that the loading efficiency of siRNA was approximately 38 % at the mass ratio of 5:1. As the mass ratio of nanoparticle-to-siRNA increased, this value sharply increased and reached a maximum of 99 % at a 20:1 ratio (Fig. 1F). Agarose gel electrophoresis was also used to characterize the concentration of residual siRNA in the solution post-synthesis. As the mass ratio of nanoparticle-to-siRNA increased, the amount of free siRNA decreased. Very little residual siRNA remained at a mass ratio of 15:1 (Fig. 1H), while no migration of free siRNA was observed at a ratio of 20:1, indicating near-complete encapsulation (Fig. 1H). Additionally, the TEM images and DLS showed that siRNA did not change the shape of BCP and PDI (Fig. 1G). The zeta potential of BCP nanoparticles decreased to −21.3 mV with the addition of siRNA (Fig. 1J). These results suggested that a 20:1 ratio was optimal for maximizing siRNA loading efficiency while minimizing waste. Therefore, subsequent experiments were conducted using this ratio.

3.2.2. siRNA transfection efficiency via BCP nanoparticles in BMSCs

Next, the transfection efficiency of siRNA in BMSCs was evaluated using Cy3-labeled siRNA. Results showed that the BMSCs in the control group exhibited almost no Cy3 fluorescence, and BMSCs in the free siRNA group showed minimal fluorescence 6 h after transfection at a siRNA concentration of 100 nM (Fig. 1K). This result indicates a very low uptake of free siRNA by BMSCs and highlights the necessity of developing carriers for more efficient siRNA delivery (Fig. 1K). The si@CaP group displayed enhanced Cy3 fluorescence, while the si@BCP group showed strong fluorescence, indicating that si@BCP significantly increased siRNA uptake (Fig. 1K). Flow cytometry measurements indicated that the Cy3-positive rate of BMSCs for the free siRNA group was 2.15 %, while the Cy3-positive rates were significantly higher, *i.e.*, 32.16 %, for the si@CaP group and 87.27 % for the si@BCP group (Fig. 1L and O i). These findings demonstrated a significant improvement in siRNA delivery efficiency with BCP, which is likely due to improved dispersibility, stability, and cellular interaction properties of BCP nanoparticles. Further, RT-qPCR analysis of MEG3 expression revealed that si@BCP reduced the relative expression of MEG3 to 36 % compared to the control, which clearly surpassed the si@CaP efficiency, which reduced the relative expression of MEG3 to only 68 % compared to the control (Fig. 1O ii). These data confirm that si@BCP significantly promotes the uptake of and transfection of siRNA and that the si@BCP nanoparticles are effective carriers for delivering siRNA to BMSCs.

3.2.3. Epigenetic regulation

Downstream epigenetic and functional changes accompany effective gene silencing. β-catenin is one of the core genes in BMSCs-mediated intramembranous ossification and bone regeneration [38]. MEG3 specifically binds to the promoter region of the β-catenin and recruits EZH2 to this area [39], thereby inhibiting β-catenin transcription [23]. IF staining of EZH2 and β-catenin protein expression showed that a more effective decrease in EZH2 expression and a more enhanced β-catenin expression was achieved when treated with si@BCP compared to treatment with si@CaP or free siRNA (Fig. 2M, N, and O). These results emphasized the potential of si@BCP to regulate epigenetic regulators and downstream signaling pathways, thereby offering possibilities for treating critical bone defects characterized by upregulated MEG3.

3.2.4. In vitro biocompatibility of si@BCP

Biocompatibility is crucial for any nanoparticle-based gene delivery system [40]. Therefore, the biocompatibility of free siRNA, si@CaP, and si@BCP was also assessed through Calcein-AM/PI staining and a CCK8 assay. Calcein-AM/PI staining after 6 h of co-culture showed no apparent cytotoxic effects in all experimental groups (Fig. S2A). CCK8 assay results also indicated no significant statistical differences in proliferation across the groups (Fig. S2B). These results ensure the safety of si@BCP for potential *in vivo* applications.

3.3. Preparation and characterization of MSOMs

3.3.1. Microfluidic fabrication of si@BCP-loaded microgels

The effective delivery and sustained release of siRNA and bioactive factors are crucial for successful tissue engineering and regeneration [41,42]. Microgels prepared using microfluidic techniques may serve as excellent nanoparticle carriers, preventing their rapid clearance *in vivo* [41]. Here, we embedded si@BCP as a secondary structure within GelMA using a microfluidic device (Fig. S3A). GelMA was synthesized and freeze-dried as previously reported [28], resulting in a white, sponge-like material (Fig. 2D-i). si@BCP nanoparticles were loaded by first dissolving the GelMA (Fig. 2D-ii) and then dispersing the si@BCP nanoparticles in the GelMA solution (Fig. 2D-iii). Microdroplets were then prepared using microfluidics (Fig. S3B and C), followed by freezing, UV cross-linking, and oil phase removal to obtain the final si@BCP-loaded microgels (si@BCP@MGs) (Fig. 2D-iv). Both microgels (MGs) and si@BCP@MGs maintained complete shapes and uniform sizes, with average diameters of approximately 198 μm (MGs) and 202 μm (si@BCP@MGs), respectively (Fig. 2A, E, and F). Both types of microgels were lyophilized for subsequent experiments. SEM images of the lyophilized microgels show that their morphology remains spherical with dense nanoparticles (white arrows) observed on the si@BCP@MGs (Fig. 2B). Cy3-labeled siRNA was loaded into BCP nanoparticles using the same method to verify the presence and distribution of si@BCP in si@BCP@MGs. The red fluorescence was confined within the microgels, indicating effective encapsulation of si@BCP in the microgel (Fig. 2C).

3.3.2. Construction of MSOMs

To achieve sustained *in situ* delivery of si@BCP to BMSCs and effectively regulate MEG3 and β-catenin expression, the MSOMs were designed to continuously release siRNA while incorporating SDF-1α to actively recruit BMSCs, thereby enabling synchronized cell recruitment and targeted gene regulation. SDF-1α was absorbed into the

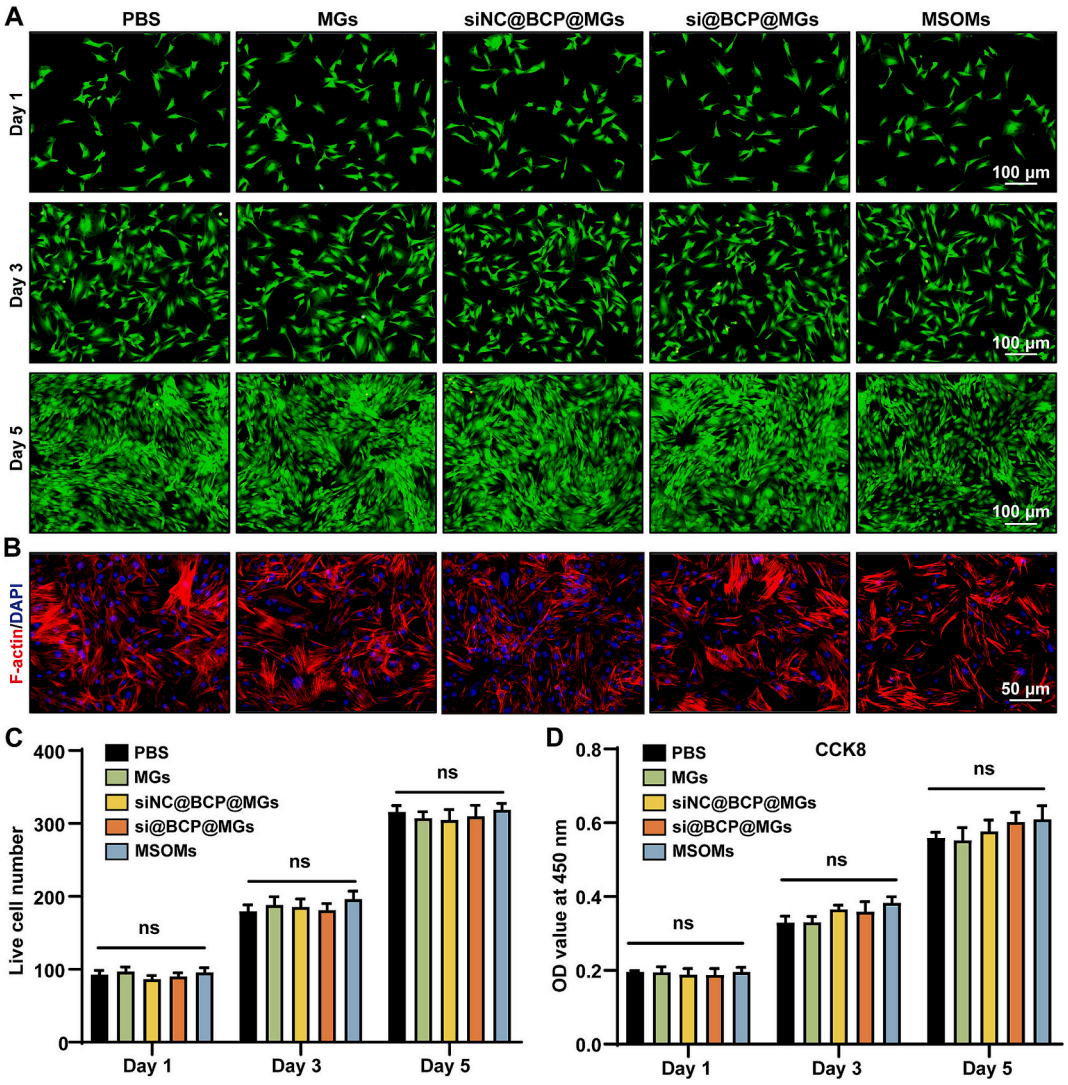

Fig. 3. *In vitro* biocompatibility of MSOMs. (A) Calcein-AM/PI staining towards BMSCs on different days. (B) F-actin and DAPI staining towards BMSCs on day 5. (C) Quantitative analysis of live cell number in Calcein-AM/PI staining. (D) CCK8 assay. All n = 3. ns indicates $p > 0.05$.

si@BCP@MGs through swelling, followed by electrostatic interactions with the si@BCP@MGs, which is a gentle process that largely preserves the stability of the growth factors [43]. There, we performed swelling tests, and the results demonstrated that the si@BCP@MGs had an excellent water absorption capacity, stabilizing at a swelling rate of 1928 % after 4 h in PBS (Fig. 2H). This high swelling capability facilitated internal fluid dynamics, aiding in the absorption and release of growth factors while maintaining the structural integrity of the microgels [44]. ELISA results showed an SDF-1α loading efficiency of 85.7 % and a capacity of 25.95 ng SDF-1α per mg si@BCP@MGs (Fig. 2G). Furthermore, FTIR spectra showed characteristic peaks at 3310 cm^{-1} for O-H/N-H stretching of GelMA, SDF-1α, and BSA [45–47] and for amide I and II bands of GelMA, SDF-1α, and BSA at 1630 cm^{-1} and 1540 cm^{-1}, respectively (Fig. 2K) [45–47]. The C—O ester peak of GelMA at 1240 cm^{-1} and the phosphate peak of si@BCP at 1078 cm^{-1} were also clearly visible [27]. These results confirm the integration of si@BCP and SDF-1α within the GelMA structure and the successful construction of MSOMs.

3.3.3. Tailored release of payloads from MSOMs to promote bone regeneration

Microgels can function as micro-scaffolds in bone regeneration [24]. During bone regeneration, SDF-1α must be rapidly released to promptly recruit BMSCs, while si@BCP requires sustained release to continuously silence MEG3 and relieve epigenetic suppression, thereby synergistically promoting stem cell recruitment and OGD. The *in vitro* release of SDF-1α from MSOMs showed a biphasic release pattern, with around 72 % released quickly in the first four days, while gradual release over the next 28 days reached a cumulative release of 96 % (Fig. 2J). This controlled release profile is advantageous for tissue engineering applications because early recruitment of BMSCs is critical for initiating repair processes, while long-term release helps sustain cell recruitment [9].

Collagenase II was employed to degrade GelMA microgels as it mimics the *in vivo* enzymatic environment, enabling controlled hydrogel breakdown and facilitating the sustained release of encapsulated nanoparticles such as si@BCP [48]. Based on this, we evaluated the degradation behavior of MGs and MSOMs, as well as the release profile of si@BCP from the MSOMs in PBS containing Collagenase II. The degradation curve of MGs showed that their initial mass reduced to approximately 79 % on Day 7, 49 % on Day 28, and 13 % on Day 56 (Fig. 2I). In contrast, MSOMs exhibited a markedly slower and more continuous degradation pattern, with 56 % of their mass remaining on Day 28 and 26 % remaining on Day 56 (Fig. 2I). Morphologically, MGs displayed evident changes as early as Day 7, with increased peripheral translucency and edge irregularities, indicating significant degradation (Fig. S3D). By Day 28, MGs had largely collapsed, and by Day 56, only

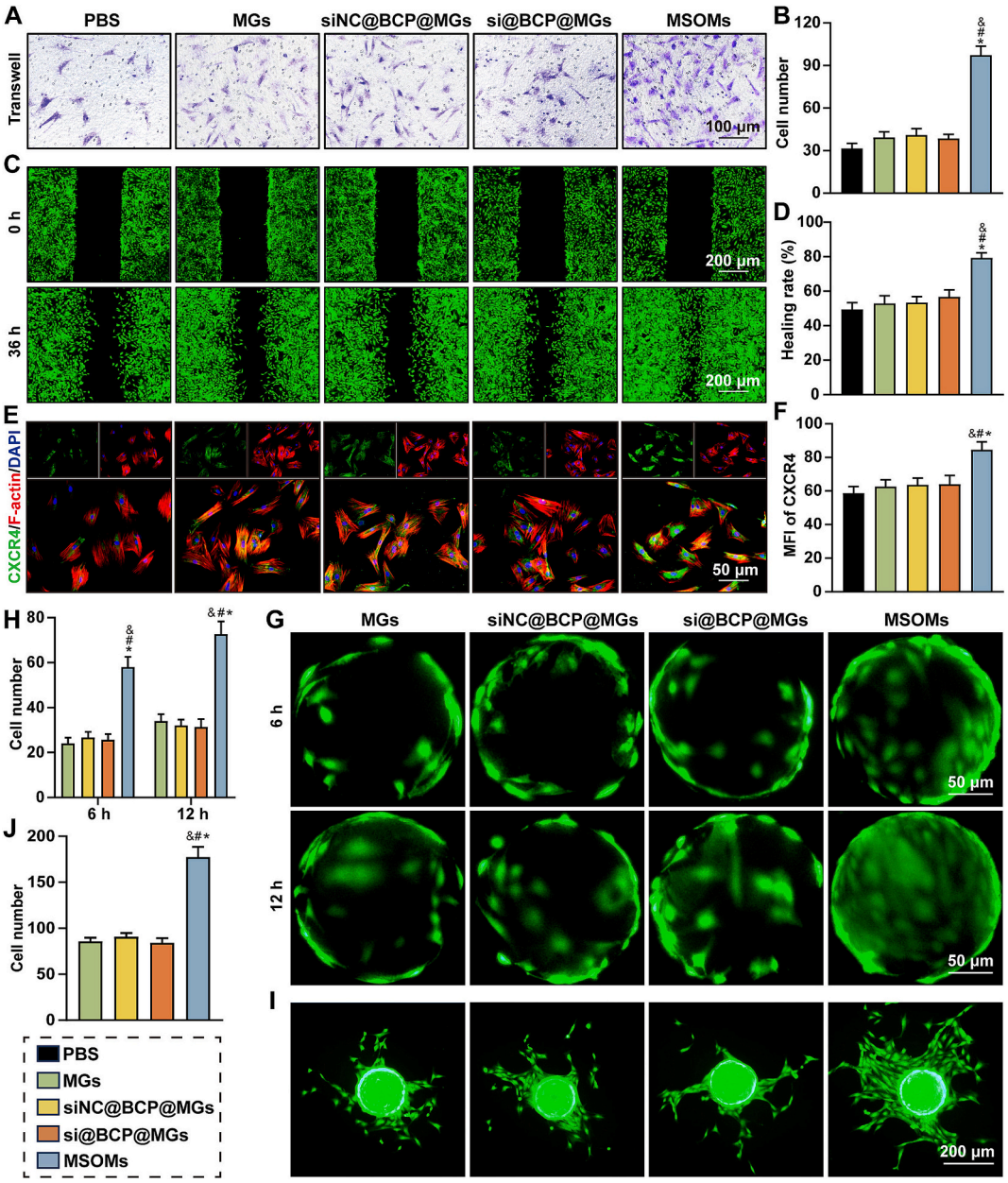

Fig. 4. The recruitment and capture of BMSCs by MSOMs. (A) Crystal violet staining was used to test the migration of BMSCs in the Transwell assay. (B) Quantitative analysis of migrated BMSCs. (C) Wound-healing assay. (D) Quantitative analysis of wound-healing percentage. (E) IF staining of CXCR4 and (F) its semi-quantitative analysis. (G) BMSCs capture assay. (H) Quantitative analysis of captured BMSCs on different microgels. (I) Proliferation of captured BMSCs with different microgels on 12-well plates. (J) Quantitative analysis of live cells in (I). All n = 3 ($p < 0.05$ was indicated by the symbols *, &, and # when compared to the MGs, siNC@BCP@MGs, and si@BCP@MGs groups, respectively). (For interpretation of the references to colour in this figure legend, the reader is referred to the web version of this article.)

minimal residues remained, with a complete loss of spherical structure. MSOMs, however, retained their morphology more effectively, maintaining spherical integrity through Day 28 and preserving partial structure even on Day 56 (Fig. 2L). The slower degradation rate of MSOMs compared to that observed for the free microgel is likely due to the structural reinforcement provided by the encapsulated si@BCP nanoparticles. Correspondingly, si@BCP release from MSOMs followed a sustained profile, with approximately 14 % released by Day 7, 45 % by Day 28, and 81 % by Day 56 (Fig. 2J). The coordinated degradation and release behavior of MSOMs ensures prolonged local delivery of siRNA, providing a temporal match between carrier disassembly and therapeutic demand.

3.4. *In vitro* biocompatibility of MSOMs

Biocompatibility is critical for bone regeneration materials to be successfully used *in vivo* [28]. We also prepared siRNA-negative control (siNC)@BCP@MGs using the same procedure as si@BCP@MGs. siNC serves as a negative control to verify that the observed therapeutic effects are specifically due to MEG3 silencing rather than nonspecific effects from the delivery system or siRNA presence. The BMSCs were divided into PBS, MGs, siNC@BCP@MGs, si@BCP@MGs, and MSOMs groups to evaluate the biocompatibility of MGs, siNC@BCP@MGs, si@BCP@MGs, and MSOMs through Calcein-AM/PI staining and CCK8 assays. Calcein-AM/PI staining data indicated that all groups could support the long-term proliferation of BMSCs with no significant

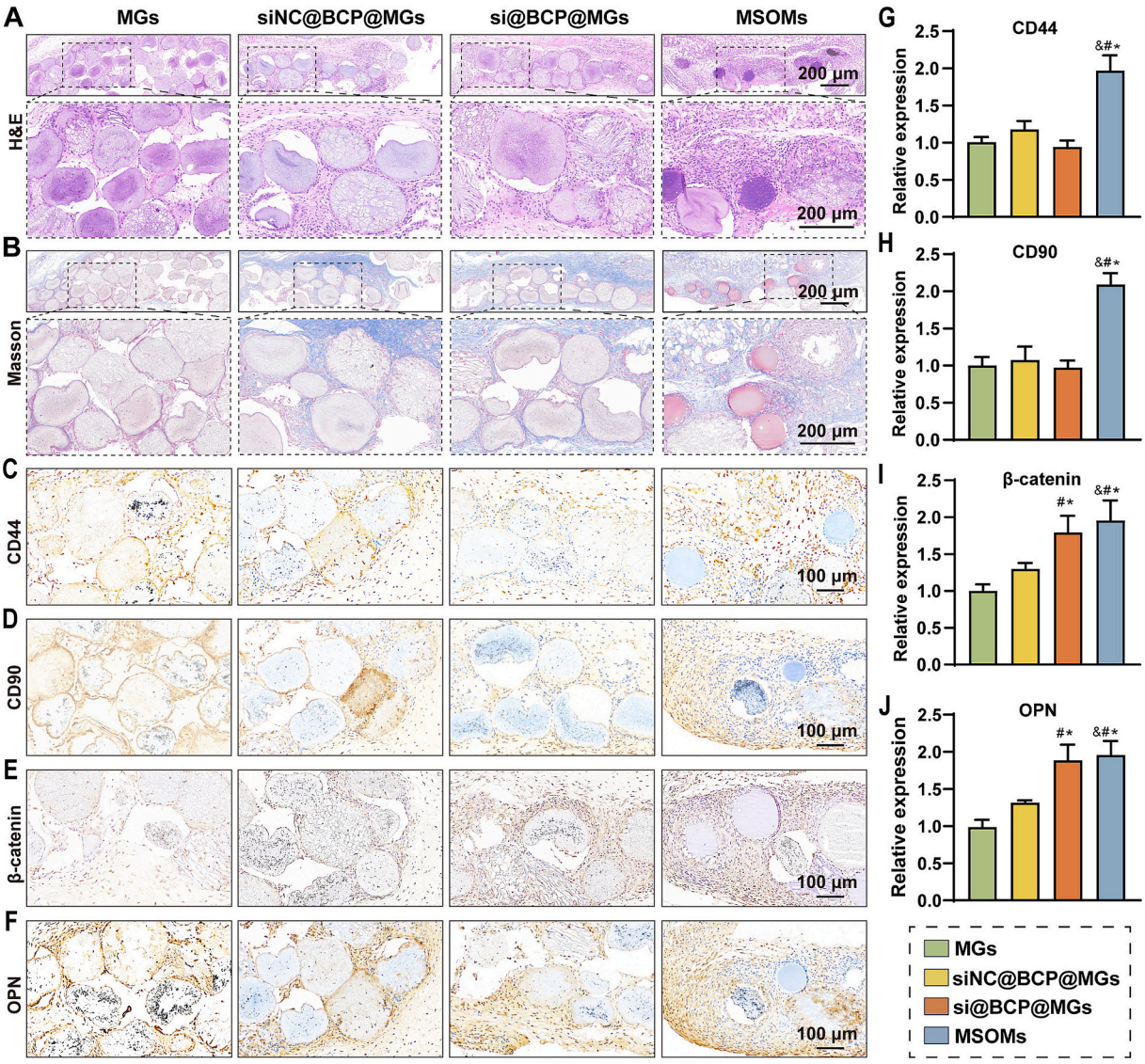

Fig. 5. *In vivo* recruitment and osteogenesis of BMSCs by MSOMs. H&E (A) and Masson trichrome (B) staining of MSOMs implanted under the periosteum for 7 days. IHC staining of CD44 (C), CD90 (D), β-catenin (E), and OPN (F), as well as the semi-quantitative analysis of corresponding positive area (G-J). All n = 3 ($p < 0.05$ was indicated by the symbols *, &, and # when compared to the MGs, siNC@BCP@MGs, and si@BCP@MGs groups, respectively).

differences among different groups (Fig. 3A and C). CCK8 assay results also demonstrated that the MGs, siNC@BCP@MGs, si@BCP@MGs, and MSOMs did not inhibit the proliferation of BMSCs (Fig. 3D). These findings confirmed that the loading of si@BCP and subsequent modifications did not induce cytotoxic effects, thus preserving the suitability of MOMS for cellular interactions and tissue integration. Furthermore, F-actin and DAPI staining showed evenly distributed cytoskeletal structures and active nuclei of BMSCs in all groups (Fig. 3B), indicating that the continuous supply of si@BCP@MGs or MSOMs provided a suitable microenvironment for the adherence and growth of BMSCs.

3.5. In vitro and in vivo evaluation on the migration and recruitment of BMSCs

3.5.1. In vitro evaluation on the migration of BMSCs

The chemotaxis of endogenous BMSCs to bone defect sites is critical in intramembranous ossification-mediated bone regeneration [9]. However, it has been confirmed that the number of BMSCs in the defect sites is insufficient [49], indicating a deficiency in natural chemotactic responses. Consequently, there is a need for biomaterials that can enhance cell recruitment and adhesion. Recent studies have explored various chemotactic factors, such as SDF-1α and platelet-derived growth factor-BB (PDGF-BB), that promote the chemotaxis of BMSCs to defect sites to enhance bone regeneration [50,51]. Wound healing assay (scratch assay) and Transwell assay were conducted to simulate the chemotaxis of MSOMs on endogenous BMSCs after injection into bone defect areas. The BMSCs were divided into PBS, MGs, siNC@BCP@MGs, si@BCP@MGs, and MSOMs groups. The Transwell assay revealed that the MSOMs group exhibited a 2.5-fold increase in migrated BMSCs than the si@BCP@MGs group (Fig. 4A and B). Similarly, the wound healing assay showed that the MSOMs group healed more than 80 % of the scratched area within 36 h, significantly better than the other groups that healed less than 40 % of the scratched area (Fig. 4C and D). SDF-1α plays a critical role in attracting BMSCs to bone defect regions through the activation of the SDF-1α/CXCR4 signaling pathway [9]. Therefore, IF staining was used to assess the expression of CXCR4 in BMSCs. A slight increase in CXCR4 expression was observed in the MGs, siNC@BCP@MGs, and si@BCP@MGs groups compared to the PBS group, while CXCR4 expression was significantly upregulated in BMSCs for the MSOMs group (Fig. 4E and F). These results indicate that the MSOM can activate the SDF-1α/CXCR4 pathway by releasing SDF-1α, thus encouraging BMSC migration to the faulty location.

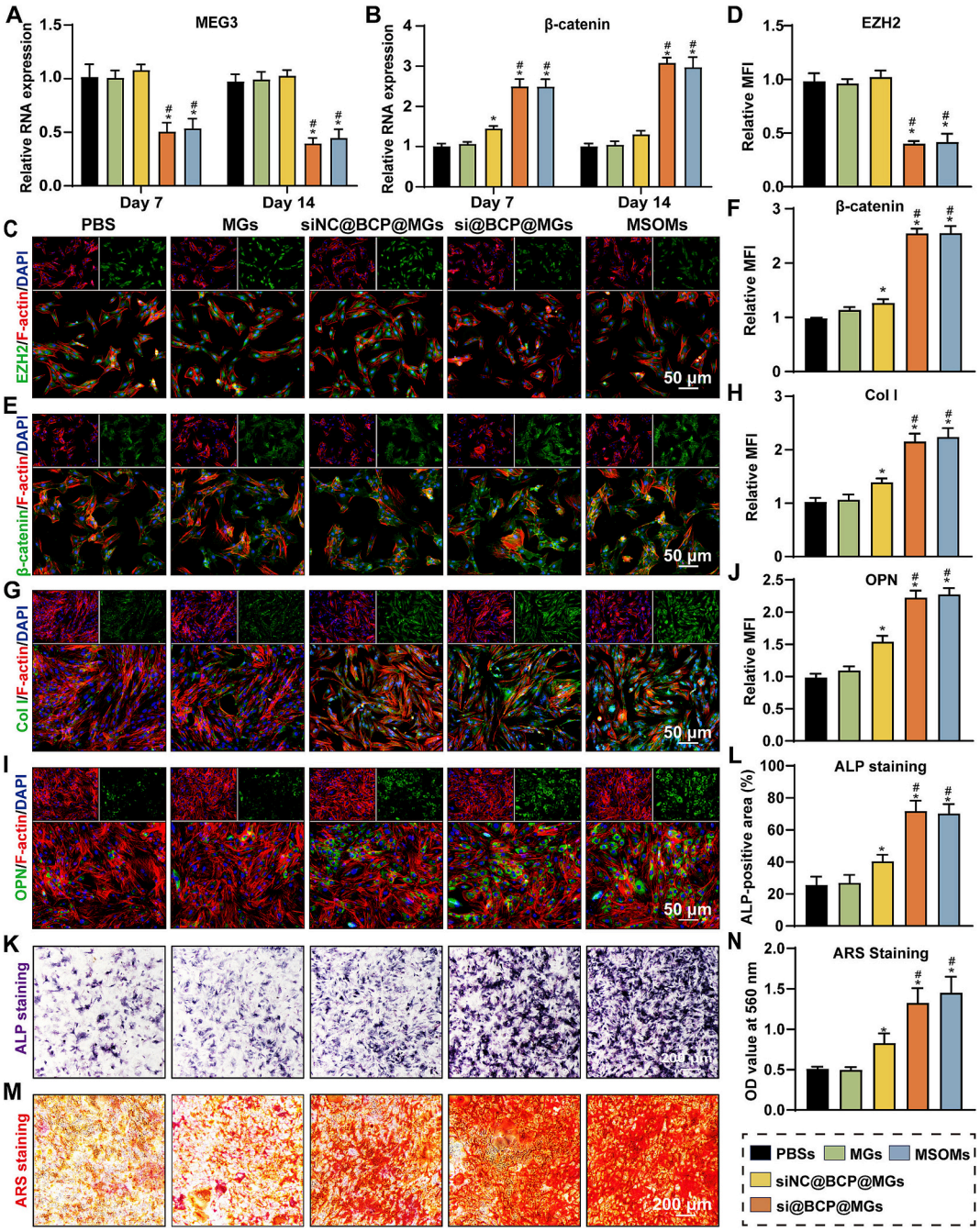

Fig. 6. *In vitro* therapy of BMSCs by MSOMs. MEG3 (A) and β-catenin mRNA (B) expression after co-culturing with different microgels. IF staining and semi-quantitative analysis of (C, D) EZH2, (E, F) β-catenin, (G, H) Col I, and (I, J) OPN. (K) ALP staining and (L) semi-quantitative analysis. (M) ARS staining and (N) quantitative analysis. All n = 3 ($p < 0.05$ was indicated by the symbols *, &, and # when compared to the MGs, siNC@BCP@MGs, and si@BCP@MGs groups, respectively).

3.5.2. *In vitro evaluation on the recruitment of BMSCs*

To further validate the capacity of MSOMs to capture endogenous BMSCs, the BMSCs were divided into MGs, siNC@BCP@MGs, si@BCP@MGs, and MSOMs groups. Each group of microgels was cultured with BMSCs in 2 mL Eppendorf (EP) tubes. After 6 h, the number of BMSCs on the surface of MSOMs was twice that of other microgels, a trend that became more pronounced after 12 h (Fig. 4G and H). Subsequently, different microgels with captured BMSCs were seeded in 12-well plates, and Calcein-AM/PI staining was performed on the third day to observe BMSC growth around different microgels. Results showed that fusiform BMSCs had fully colonized the microgels and migrated radially onto the plates, with BMSCs on the MSOMs showing broader dispersion, significantly higher than the other three microgels (Fig. 4I and J).

3.5.3. *In vivo evaluation on the recruitment of BMSCs*

To validate the capability of MSOMs to recruit BMSCs *in vivo*, SD rats were divided into MGs, siNC@BCP@MGs, si@BCP@MGs, and MSOMs groups. The four types of microgels were injected into the subperiosteal region of the rat cranial bone, and samples were harvested after one week. H&E and Masson's trichrome staining confirmed the biocompatibility of the microgels by showing no adverse effects on the periosteum and subcutaneous tissue structures (Fig. 5A and B). CD44 and CD90, which are common markers for BMSCs [52], were evaluated *via*

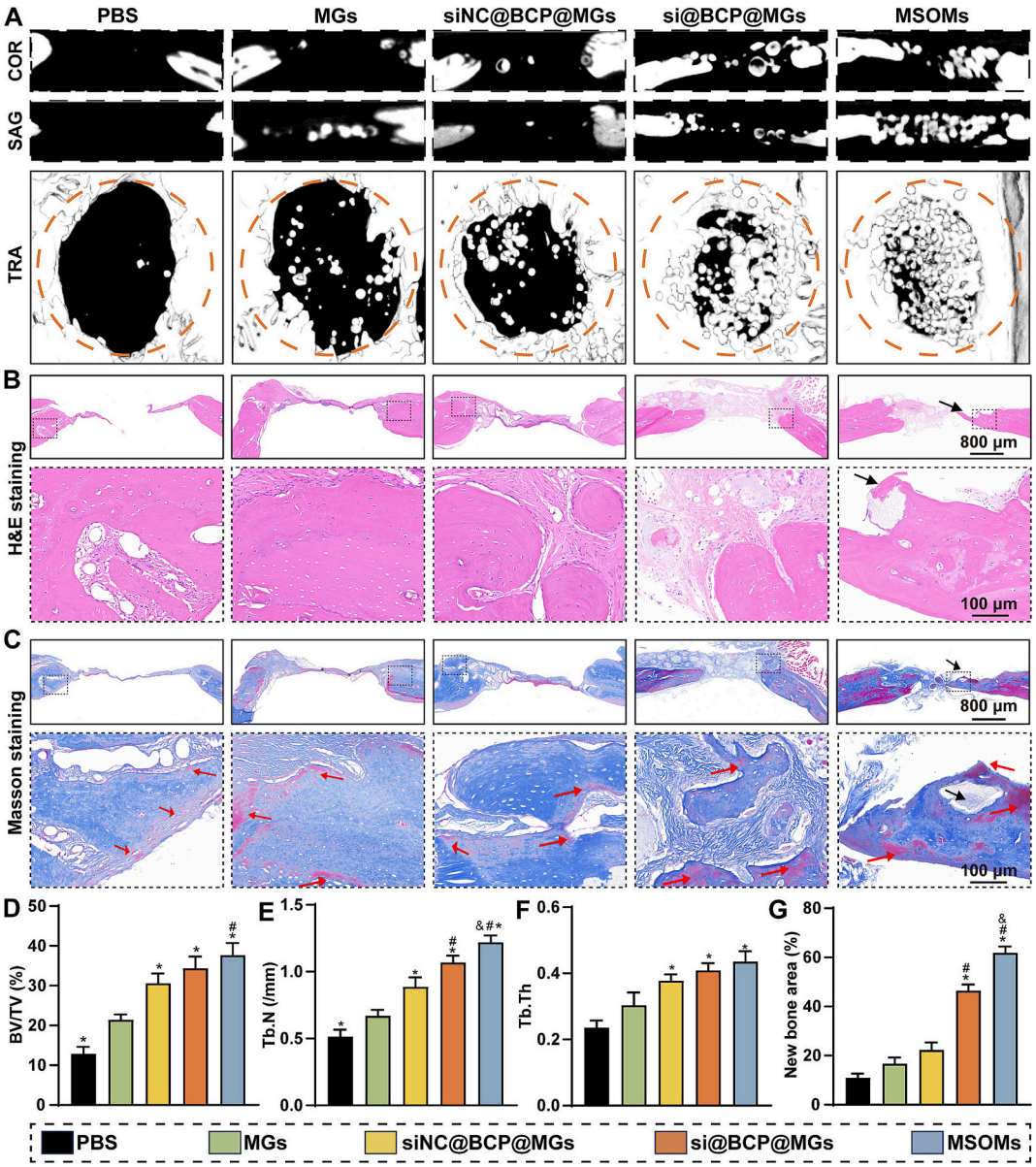

Fig. 7. Formation of ossification center *in vivo*. (A) MicroCT of the skull defect area 8 weeks after surgery (COR, coronal; SAG, sagittal; TRA, transverse). H&E (B) and Masson trichrome staining (C) (black arrows indicate the formation of ossification centers around the MSOMs, and the red areas indicated by the red arrows are mature mineralized bone tissues). Semi-quantitative analysis data of BV/TV (D), Tb.N (E), Tb.Th (F), and percentage of new bone area (G). All n = 3 ($p < 0.05$ was indicated by the symbols *, &, and # when compared to the MGs, siNC@BCP@MGs, and si@BCP@MGs groups, respectively). (For interpretation of the references to colour in this figure legend, the reader is referred to the web version of this article.)

IHC staining. The findings demonstrated that MSOMs considerably increased BMSC recruitment, as evidenced by a doubling of CD44 and CD90 expression compared to the MGs group (Fig. 5C, D, G, and H). These *in vivo* findings suggested that the MSOMs can recruit BMSCs and provide a favorable environment for their adhesion, dispersion, and proliferation, thereby making MSOMs suitable for treating bone defects.

3.6. Epigenetic regulation of MSOMs in vitro and in vivo

The capacity of MSOMs to silence MEG3 and upregulate β-catenin mRNA in BMSCs was confirmed through a Transwell co-culture system. The BMSCs were divided into PBS, MGs, siNC@BCP@MGs, si@BCP@MGs, and MSOMs groups. RT-qPCR analysis showed that, compared to the siNC@BCP@MGs, the MSOMs reduced the expression of MEG3 by approximately 50 % and 60 % on days 7 and 14, respectively, while increasing β-catenin mRNA level by 2.5 to 3-fold during the same period (Fig. 6A and B). IF staining further validated these results by demonstrating downregulation of EZH2 protein expression and a significant upregulation of β-catenin protein expression, which exceeded a 2-fold increase in the MSOMs group (Fig. 5C-F). Additionally, experiments on subperiosteal implantation of microgels revealed that MSOMs markedly increased β-catenin expression by 1.8-fold compared to the MGs and siNC@BCP@MGs groups (Fig. 5E and I). These results of epigenetic regulation underscore the effectiveness of MSOMs in reversing MEG3-mediated suppression of β-catenin, which is a critical gene for intramembranous ossification and new bone formation [38].

3.7. MSOMs effect on the OGD formation in vitro

To evaluate the effects of MSOMs on OGD, the BMSCs were divided into PBS, MGs, siNC@BCP@MGs, si@BCP@MGs, and MSOMs groups, and each group of microgels was co-cultured with BMSCs in a Transwell

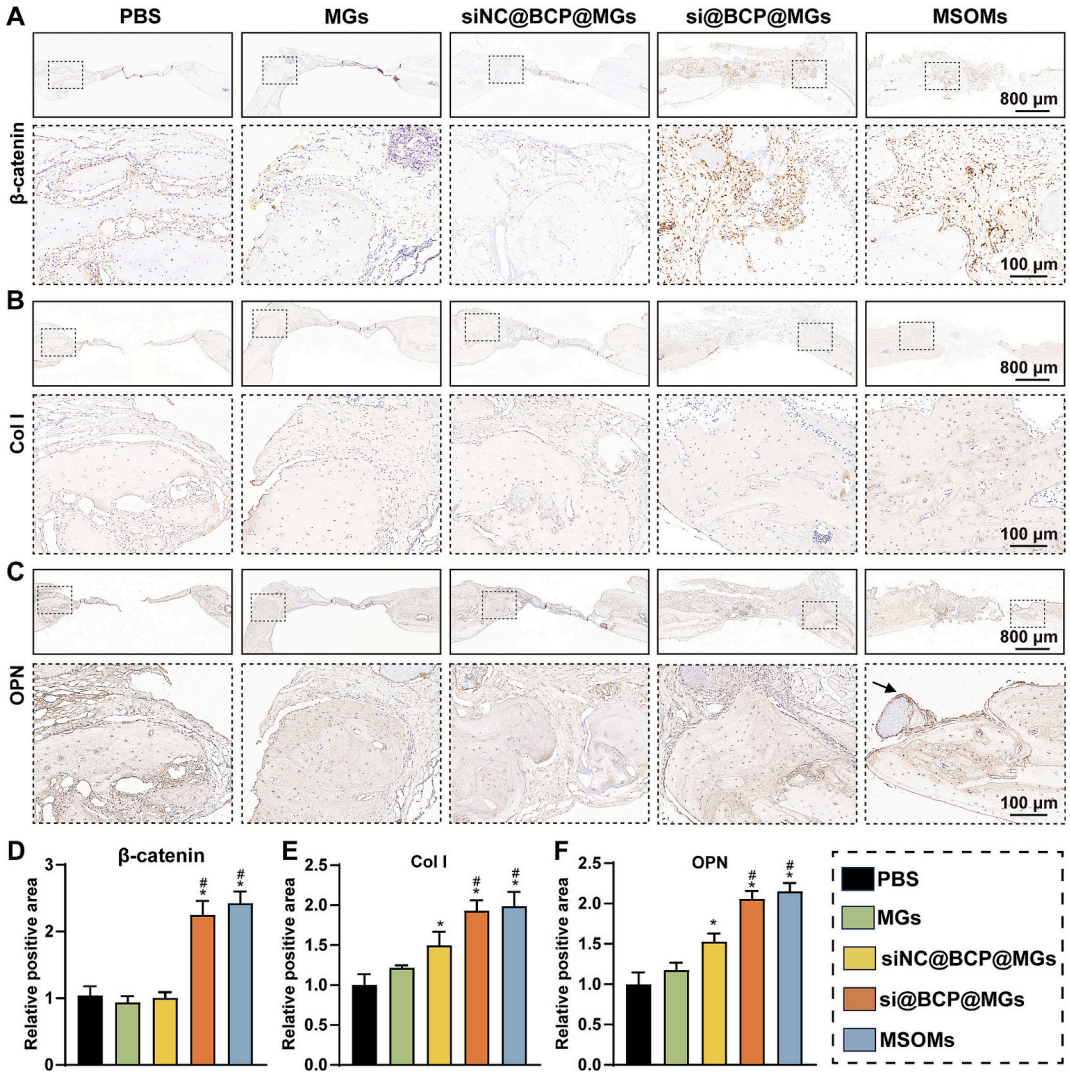

Fig. 8. Epigenetic regulation and osteogenic differentiation by the MSOMs *in vivo*. IHC staining of β-catenin (A), Col I (B), and OPN (C). The black arrow indicates the formation of ossification centers around the MSOMs. (D)-(F) Semi-quantitative analysis of relative β-catenin-positive area (D), relative Col I-positive area (E), and relative OPN-catenin-positive area (F). All n = 3 ($p < 0.05$ was indicated by the symbols *, &, and # when compared to the MGs, siNC@BCP@MGs, and si@BCP@MGs groups, respectively).

system to induce OGD. Collagen Type I (Col I) is the primary matrix protein and a major component of the extracellular matrix (ECM) of bone, and it is an important biomarker for assessing early intramembranous ossification [53,54]. Osteopontin (OPN) is a vital marker for assessing mid-to-late-stage OGD. It is crucial in intramembranous ossification and is primarily associated with mineralization [55,56]. IF staining revealed that MSOM significantly upregulated the expression of OPN and Col I by more than 2-fold compared to other groups (Fig. 6G-J). Moreover, experiments on subperiosteal implantation of microgels revealed that OPN expression was markedly higher in the si@BCP@MGs and MSOMs groups than in the MGs and siNC@BCP@MGs groups (Fig. 5F and J). One early indicator of OGD is alkaline phosphatase (ALP), which catalyzes the hydrolysis of phosphate groups, aiding in the generation of inorganic phosphate during the early stages of bone mineralization [57]. Alizarin Red S (ARS) staining for detecting calcium deposition is a classic marker of intramembranous ossification [58]. ALP staining conducted after 7 days of OGD revealed that the ALP activity of the MSOMs group had significantly increased, with positive areas approaching 70 % (Fig. 6K and L). A similar trend was observed with ARS staining, indicating increased calcium deposition in the later stages of OGD (Fig. 6M and N). Interestingly, compared to those in the PBS and MGs groups, BMSCs in the siNC@BCP@MGs group also exhibited significantly enhanced OGD, as demonstrated by IF staining for Col I and OPN, ALP staining, and ARS staining (Fig. 6H-N). This intriguing result may be attributed to the sustained release of Ca^{2+} and PO_4^{3-} from the siNC@BCP@MGs group, which promotes extracellular matrix mineralization and upregulates the expression of osteogenic markers such as ALP and OPN [59]. These results highlighted how MSOMs created a favorable microenvironment for intramembranous ossification by regulating gene expression, further solidifying its potential as a therapeutic ossification micro-unit.

3.8. MSOMs promote bone regeneration in vivo

3.8.1. MSOMs significantly enhance bone regeneration in a rat cranial defect model

To assess the therapeutical effectiveness of MSOMs *in vivo*, a 5 mm cranial defect model was established in SD rats based on a previous study [60], and these rats were divided into PBS, MGs, siNC@BCP@MGs, si@BCP@MGs, and MSOMs groups. Various microgels were implanted to assess the potential of MSOMs to promote bone regeneration *in vivo*. Micro-CT analysis demonstrated that all microgel treatment groups exhibited higher bone regeneration two months after implantation than the PBS group, with MSOMs showing the highest

repair effects (Fig. 7A). Quantitative measurements of BV/TV (Fig. 7D), Tb.N (Fig. 7E), and Tb.Th (Fig. 7F) further confirmed the superior regenerative performance of the MSOMs group. These findings indicated that the MSOMs effectively promoted bone regeneration *in vivo*.

3.8.2. Histological evaluation confirms MSOMs-driven intramembranous ossification

Histological staining further confirmed the potential of MSOMs to enhance intramembranous ossification. H&E staining across all microgel groups revealed no signs of inflammation or necrosis (Fig. 7B), thereby indicating that the MSOMs system was well tolerated and did not elicit adverse immune reactions, thus making it a suitable candidate for clinical translation. Masson's trichrome staining revealed that the MSOMs group exhibited robust new bone formation and collagen mineralization (Fig. 7C and G, red arrows). However, the PBS and MGs groups demonstrated limited new bone formation with substantial fibrous connective tissue proliferation, indicative of incomplete healing (Fig. 7C and G). The new bone formation was much greater in the siNC@BCP@MGs and si@BCP@MGs groups than in the PBS and MGs groups, although it fell short of the values of the MSOMs group. Interestingly, the formation of ossification centers was noted around the MSOMs (Black arrows in Fig. 7B and C), which suggests that MSOMs created a local microenvironment conducive to osteoblast activity and bone matrix deposition to support bone formation. These results demonstrated that the MSOMs significantly and most efficiently enhanced bone repair compared to the other groups and that the efficiency decreased in the order si@BCP@MGs > siNC@BCP@MGs > MGs > PBS groups, further corroborating the microCT findings.

3.8.3. MSOMs lifts epigenetic suppression to enhance osteogenesis in vivo

IHC staining was employed to examine β-catenin, Col I, and OPN expression to validate further the capacity of MSOMs to lift epigenetic suppression of β-catenin and promote intramembranous ossification *in vivo*. Significant upregulation of β-catenin protein was observed in both the si@BCP@MGs and MSOMs groups compared to the PBS group, which is similar to the *in vitro* results (Fig. 8A and D). The MSOMs sustainably silenced MEG3 *via* the release of si@BCP, consequently effectively lifting the suppression of β-catenin expression and activating critical osteogenic pathways essential for bone repair. IHC staining demonstrated that Col I and OPN were markedly increased in the si@BCP@MGs and MSOMs groups (Fig. 8B, C, E, and F). Notably, the MSOMs group exhibited the highest Col I and OPN protein expression levels, indicating stronger OGD and bone matrix deposition capabilities. Additionally, the siNC@BCP@MGs group showed moderate expression levels of these markers, which suggests that the BCP@MGs system possessed intrinsic osteogenic properties. However, the significantly higher expression levels in the si@BCP@MGs and MSOMs groups underscored the crucial role of MEG3 silencing in enhancing the osteogenic capacity of the microgels. All *in vivo* findings suggest that the MSOMs significantly promote bone repair. Therefore, *in situ* injectable MSOMs represent a promising bone tissue engineering therapeutic strategy.

4. Conclusion

In summary, the MSOM developed in this study achieves sustained MEG3 silencing and effective BMSC recruitment, thereby relieving epigenetic suppression of β-catenin and promoting intramembranous ossification at critical bone defect sites. Through the integration of microfluidic fabrication, BCP nanoparticle stabilization, and SDF-1α-mediated chemotaxis, MSOM addresses key limitations of traditional delivery systems—such as low retention and short therapeutic duration—while simultaneously improving BMSC availability, maintaining long-term epigenetic modulation, and supporting mineralization. By bridging microscale gene regulation with macroscale repair needs, this strategy offers a precise and effective approach to bone regeneration with strong translational potential.

CRediT authorship contribution statement

Wu Yang: Writing – original draft, Investigation. **Tao Ding:** Writing – original draft, Investigation. **Pengzhen Zhuang:** Writing – original draft, Investigation. **Yu Chen:** Investigation. **Yu Zhang:** Investigation. **Zehao Chen:** Investigation. **Minjie Fan:** Investigation. **Tapani Viitala:** Writing – review & editing. **Zhongmin Wang:** Writing – review & editing. **Wenguo Cui:** Conceptualization, Supervision. **Hongbo Zhang:** Conceptualization, Supervision.

Declaration of competing interest

The authors declare no conflicts of interest.

Acknowledgment

Wu Yang, Tao Ding, and Pengzhen Zhuang contributed equally to this work. This work was supported by the National Natural Science Foundation of China (52403192 and W2411085), the Science and Technology Commission of Shanghai Municipality (22YF1441800), the Research Project (347897), Solution for Health Profile (336355), In-FLAMES Flagship (337531) grants and Printed Intelligence Infrastructure (PII-FIRI) from Research Council of Finland. This study is part of the activities of the Åbo Akademi University Foundation (SÅA) funded Center of Excellence in Research "Materials-driven solutions for combating antimicrobial resistance (MADNESS)" at ÅAU. Wu Yang (CSC202207960009) and Minjie Fan (CSC202408320125) were sponsored by the China Scholarship Council.

Appendix A. Supplementary data

Supplementary data to this article can be found online at https://doi.org/10.1016/j.jconrel.2025.113978.

Data availability

Data will be made available on request.

References

[1] C. Yan, P. Zhang, Q. Qin, K. Jiang, Y. Luo, C. Xiang, J. He, L. Chen, D. Jiang, W. Cui, 3D-printed bone regeneration scaffolds modulate bone metabolic homeostasis through vascularization for osteoporotic bone defects, Biomaterials 311 (2024) 122699.
[2] Z. Zhao, G. Li, H. Ruan, K. Chen, Z. Cai, G. Lu, R. Li, L. Deng, M. Cai, W. Cui, Capturing magnesium ions via microfluidic hydrogel microspheres for promoting cancellous bone regeneration, ACS Nano 15 (2021) 13041–13054.
[3] X. Yuan, W. Zhu, Z. Yang, N. He, F. Chen, X. Han, K. Zhou, Recent advances in 3D printing of smart scaffolds for bone tissue engineering and regeneration, Adv. Mater. 36 (2024) 2403641.
[4] Z. Zhao, R. Li, H. Ruan, Z. Cai, Y. Zhuang, Z. Han, M. Zhang, W. Cui, M. Cai, Biological signal integrated microfluidic hydrogel microspheres for promoting bone regeneration, Chem. Eng. J. 436 (2022) 135176.
[5] Q. Fan, J. Bai, H. Shan, Z. Fei, H. Chen, J. Xu, Q. Ma, X. Zhou, C. Wang, Implantable blood clot loaded with BMP-2 for regulation of osteoimmunology and enhancement of bone repair, Bioact. Mater. 6 (2021) 4014–4026.
[6] X. Han, M. Sun, B. Chen, Q. Saiding, J. Zhang, H. Song, L. Deng, P. Wang, W. Gong, W. Cui, Lotus seedpod-inspired internal vascularized 3D printed scaffold for bone tissue repair, Bioact. Mater. 6 (2021) 1639–1652.
[7] Y. Qin, Z. Jing, D. Zou, Y. Wang, H. Yang, K. Chen, W. Li, P. Wen, Y. Zheng, A metamaterial scaffold beyond modulus limits: enhanced osteogenesis and angiogenesis of critical bone defects, Nat. Commun. 16 (2025) 2180.
[8] G.N. Duda, S. Geissler, S. Checa, S. Tsitsilonis, A. Petersen, K. Schmidt-Bleek, The decisive early phase of bone regeneration, Nat. Rev. Rheumatol. 19 (2023) 78–95.
[9] Y. Mao, Y. Chen, W. Li, Y. Wang, J. Qiu, Y. Fu, J. Guan, P. Zhou, Physiology-inspired multilayer nanofibrous membranes modulating endogenous stem cell recruitment and osteo-differentiation for staged bone regeneration, Adv. Healthc. Mater. 11 (2022) 2201457.
[10] Y. He, F. Li, P. Jiang, F. Cai, Q. Lin, M. Zhou, H. Liu, F. Yan, Remote control of the recruitment and capture of endogenous stem cells by ultrasound for in situ repair of bone defects, Bioact. Mater. 21 (2023) 223–238.

[11] S.K.-H. Chow, Q. Gao, A. Pius, M. Morita, Y. Ergul, M. Murayama, I. Shinohara, M. S. Cekuc, C. Ma, Y. Susuki, The advantages and shortcomings of stem cell therapy for enhanced bone healing, Tissue Eng. C Methods 30 (2024) 415–430.
[12] S.P. Adithya, K. Balagangadharan, N. Selvamurugan, Epigenetic modifications of histones during osteoblast differentiation, Biochim. Biophys. Acta Gene Regul. Mech. 1865 (2022) 194780.
[13] M. Ghorbaninejad, M. Khademi-Shirvan, S. Hosseini, M. Baghaban Eslaminejad, Epidrugs: novel epigenetic regulators that open a new window for targeting osteoblast differentiation, Stem Cell Res Ther 11 (2020) 1–14.
[14] S. Kootala, D. Ossipov, J.J. van den Beucken, S. Leeuwenburgh, J. Hilborn, Bisphosphonate-functionalized hyaluronic acid showing selective affinity for osteoclasts as a potential treatment for osteoporosis, Biomater. Sci. 3 (2015) 1197–1207.
[15] Y. Zhao, J. He, T. Qiu, H. Zhang, L. Liao, X. Su, Epigenetic therapy targeting bone marrow mesenchymal stem cells for age-related bone diseases, Stem Cell Res Ther 13 (2022) 201.
[16] Y. Chen, Y. Sun, X. Xue, H. Ma, Comprehensive analysis of epigenetics mechanisms in osteoporosis, Front. Genet. 14 (2023) 1153585.
[17] W. Chang, B. Tian, Q. Qin, D. Li, Y. Zhang, C. Zhou, B. Wu, M. Zhang, H. Shan, Y. Ni, Receptor activator of nuclear factor kappa-B-expressing mesenchymal stem cells-derived extracellular vesicles for osteoporosis therapy, ACS Nano 18 (2024) 35368–35382.
[18] F. Wang, Q. Wang, Y. Zhao, Z. Tian, S. Chang, H. Tong, N. Liu, S. Bai, X. Li, J. Fan, Adipose-derived stem cells with miR-150-5p inhibition laden in hydroxyapatite/tricalcium phosphate ceramic powders promote osteogenesis via regulating Notch3 and activating FAK/ERK and RhoA, Acta Biomater. 155 (2023) 644–653.
[19] J. Cao, Q. Zhang, Q. Yang, Y. Yu, M. Meng, J. Zou, Epigenetic regulation of osteogenic differentiation of periodontal ligament stem cells in periodontitis, Oral Dis. 29 (2023) 2529–2537.
[20] S. Farhadova, A. Ghousein, F. Charon, C. Surcis, M. Gomez-Velazques, C. Roidor, F. Di Michele, M. Borensztein, A. De Sario, C. Esnault, The long non-coding RNA Meg3 mediates imprinted gene expression during stem cell differentiation, Nucleic Acids Res. 52 (2024) 6183–6200, gkae247.
[21] Y.B. Liu, L.P. Lin, R. Zou, Q.H. Zhao, F.Q. Lin, Silencing long non-coding RNA MEG3 accelerates tibia fraction healing by regulating the Wnt/β-catenin signalling pathway, J. Cell. Mol. Med. 23 (2019) 3855–3866.
[22] Q. Wang, Y. Li, Y. Zhang, L. Ma, L. Lin, J. Meng, L. Jiang, L. Wang, P. Zhou, Y. Zhang, LncRNA MEG3 inhibited osteogenic differentiation of bone marrow mesenchymal stem cells from postmenopausal osteoporosis by targeting miR-133a-3p, Biomed. Pharmacother. 89 (2017) 1178–1186.
[23] L. Deng, H. Hong, X. Zhang, D. Chen, Z. Chen, J. Ling, L. Wu, Down-regulated lncRNA MEG3 promotes osteogenic differentiation of human dental follicle stem cells by epigenetically regulating Wnt pathway, Biochem. Biophys. Res. Commun. 503 (2018) 2061–2067.
[24] S. Chen, X. Han, Y. Cao, W. Yi, Y. Zhu, X. Ding, K. Li, J. Shen, W. Cui, D. Bai, Spatiotemporalized hydrogel microspheres promote vascularized osteogenesis via ultrasound oxygen delivery, Adv. Funct. Mater. 34 (2024) 2308205.
[25] R. Khalifehzadeh, H. Arami, Biodegradable calcium phosphate nanoparticles for cancer therapy, Adv. Colloid Interf. Sci. 279 (2020) 102157.
[26] M. Nakamura, A. Oyane, Y. Shimizu, S. Miyata, A. Saeki, H. Miyaji, Physicochemical fabrication of antibacterial calcium phosphate submicrospheres with dispersed silver nanoparticles via coprecipitation and photoreduction under laser irradiation, Acta Biomater. 46 (2016) 299–307.
[27] B. Sun, M. Gillard, Y. Wu, P. Wu, Z.P. Xu, W. Gu, Bisphosphonate stabilized calcium phosphate nanoparticles for effective delivery of plasmid DNA to macrophages, ACS Appl. Bio Mater. 3 (2020) 986–996.
[28] P. Zhuang, W. Yang, Y. Zhang, Y. Chen, T. Ding, Y. Chen, F. Wang, J. Rosenholm, Y. Li, H. Zhang, In situ generating CO gas for destroying bacterial biofilms, Nano Today 56 (2024) 102296.
[29] T. Ding, Y. Xiao, Q. Saiding, X. Li, G. Chen, T. Zhang, J. Ma, W. Cui, Capture and storage of cell-free DNA via bio-informational hydrogel microspheres, Adv. Mater. 36 (2024) 2403557.
[30] X. Li, X. Li, J. Yang, J. Lin, Y. Zhu, X. Xu, W. Cui, Living and injectable porous hydrogel microsphere with paracrine activity for cartilage regeneration, Small 19 (2023) 2207211.
[31] A.J. Smith, R.E. Clutton, E. Lilley, K.E.A. Hansen, T. Brattelid, PREPARE: guidelines for planning animal research and testing, Lab. Anim. 52 (2018) 135–141.
[32] C. Qiu, Y. Wu, Q. Guo, Q. Shi, J. Zhang, Y. Meng, F. Xia, J. Wang, Preparation and application of calcium phosphate nanocarriers in drug delivery, Mater. Today Bio 17 (2022) 100501.
[33] Y.-W. Chao, Y.-L. Lee, C.-S. Tseng, L.U.-H. Wang, K.-C. Hsia, H. Chen, J.-M. Fustin, S. Azeem, T.-T. Chang, C.-Y. Chen, Improved CaP nanoparticles for nucleic acid and protein delivery to neural primary cultures and stem cells, ACS Nano 18 (2024) 4822–4839.
[34] J. Yan, X. Ma, D. Liang, M. Ran, D. Zheng, X. Chen, S. Zhou, W. Sun, X. Shen, H. Zhang, An autocatalytic multicomponent DNAzyme nanomachine for tumor-specific photothermal therapy sensitization in pancreatic cancer, Nat. Commun. 14 (2023) 6905.
[35] W. Maniukiewicz, J. Bojarska, L. Sieroń, Analysis of supramolecular interactions in alendroniate alkali metal salts: synthesis, structure, and properties of novel sodium alendronate polymorph, Struct. Chem. 29 (2018) 1525–1531.
[36] G. Güler, M.M. Vorob'ev, V. Vogel, W. Mäntele, Proteolytically-induced changes of secondary structural protein conformation of bovine serum albumin monitored by Fourier transform infrared (FT-IR) and UV-circular dichroism spectroscopy, Spectrochim. Acta A Mol. Biomol. Spectrosc. 161 (2016) 8–18.
[37] C. Li, Y. Du, H. Lv, J. Zhang, P. Zhuang, W. Yang, Y. Zhang, J. Wang, W. Cui, W. Chen, Injectable amphipathic artesunate prodrug-hydrogel microsphere as gene/drug nano-microplex for rheumatoid arthritis therapy, Adv. Funct. Mater. 32 (2022) 2206261.
[38] L. Hu, W. Chen, A. Qian, Y.-P. Li, Wnt/β-catenin signaling components and mechanisms in bone formation, homeostasis, and disease, Bone Res. 12 (2024) 39.
[39] P. Dashti, E.A. Lewallen, J.A. Gordon, M.A. Montecino, J.R. Davie, G.S. Stein, J. P. van Leeuwen, B.C. van der Eerden, A.J. van Wijnen, Epigenetic regulators controlling osteogenic lineage commitment and bone formation, Bone 181 (2024) 117043.
[40] Z. Zhao, H. Ruan, A. Chen, W. Xiong, M. Zhang, M. Cai, W. Cui, Genetic engineered ultrasound-triggered injectable hydrogels for promoting bone reconstruction, Research 6 (2023) 0221.
[41] L. Chen, J. Zhang, J. Wang, J. Lin, X. Luo, W. Cui, Inflammation-regulated auto aggregated hydrogel microspheres via anchoring cartilage deep matrix for genes delivery, Adv. Funct. Mater. 33 (2023) 2305635.
[42] J. Liu, L. Chen, Z. Sun, Z. Tao, V. Pavel, Y. Li, F. Wang, W. Cui, S. Liu, Unidirectional gene delivery electrospun fibrous membrane via charge repulsion for tendon repair, Bioact. Mater. 37 (2024) 191–205.
[43] Z. Chen, Z. Lv, Y. Zhuang, Q. Saiding, W. Yang, W. Xiong, Z. Zhang, H. Chen, W. Cui, Y. Zhang, Mechanical signal-tailored hydrogel microspheres recruit and train stem cells for precise differentiation, Adv. Mater. 35 (2023) 2300180.
[44] Y. Lei, Y. Wang, J. Shen, Z. Cai, Y. Zeng, P. Zhao, J. Liao, C. Lian, N. Hu, X. Luo, Stem cell-recruiting injectable microgels for repairing osteoarthritis, Adv. Funct. Mater. 31 (2021) 2105084.
[45] G. Hassanshahi, A. Jafarzadeh, A.J. Dickson, Expression of stromal derived factor alpha (SDF-1α) by primary hepatocytes following isolation and heat shock stimulation, Iran. J. Allergy Asthma Immunol. (2008) 61–68.
[46] S. Ramesh, M. Ramalingam, Aqueous-mediated synthesis and characterization of gelatin methacryloyl for biomedical applications, Biointerface Res. Appl. Chem. 12 (2022) 6269–6279.
[47] C. Guo, X. Guo, W. Chu, N. Jiang, H. Li, Spectroscopic study of conformation changes of bovine serum albumin in aqueous environment, Chin. Chem. Lett. 30 (2019) 1302–1306.
[48] X. Li, X. Li, J. Yang, Y. Du, L. Chen, G. Zhao, T. Ye, Y. Zhu, X. Xu, L. Deng, In situ sustained macrophage-targeted nanomicelle–hydrogel microspheres for inhibiting osteoarthritis, Research 6 (2023) 0131.
[49] J. Wei, X. Xia, S. Xiao, S. Jin, Q. Zou, Y. Zuo, Y. Li, J. Li, Sequential dual-biofactor release from the scaffold of mesoporous HA microspheres and PLGA matrix for boosting endogenous bone regeneration, Adv. Healthc. Mater. 12 (2023) 2300624.
[50] Y. Dang, Y. Zhang, G. Luo, D. Li, Y. Ma, Y. Xiao, L. Xiao, X. Wang, The decisive early phase of biomaterial-induced bone regeneration, Appl. Mater. Today 38 (2024) 102236.
[51] L. Chen, C. Yu, Y. Xiong, K. Chen, P. Liu, A.C. Panayi, X. Xiao, Q. Feng, B. Mi, G. Liu, Multifunctional hydrogel enhances bone regeneration through sustained release of stromal cell-derived factor-1α and exosomes, Bioact. Mater. 25 (2023) 460–471.
[52] X. Sun, Y. Lin, X. Zhong, C. Fan, Z. Liu, X. Chen, Z. Luo, J. Wu, S. Tima, Z. Zhang, Alendronate-functionalized polymeric micelles target icaritin to bone for mitigating osteoporosis in a rat model, J. Control. Release 376 (2024) 37–51.
[53] P. Alamán-Díez, E. García-Gareta, M. Arruebo, M.Á. Pérez, A bone-on-a-chip collagen hydrogel-based model using pre-differentiated adipose-derived stem cells for personalized bone tissue engineering, J. Biomed. Mater. Res. A 111 (2023) 88–105.
[54] B. Tian, H. Wang, Y. Zhang, J. Lv, D. Li, C. Zhou, J. Xu, Y. Ni, B. Wu, M. Zhang, Tryptophan-producing bacteria to mitigate osteoporosis and intestinal dysfunction, Bioact. Mater. 51 (2025) 293–305.
[55] S. Chawla, A. Sharma, A. Bandyopadhyay, S. Ghosh, Developmental biology-inspired strategies to engineer 3D bioprinted bone construct, ACS Biomater. Sci. Eng. 4 (2018) 3545–3560.
[56] H. Shan, X. Zhou, B. Tian, C. Zhou, X. Gao, C. Bai, B. Shan, Y. Zhang, S. Sun, D. Sun, Gold nanorods modified by endogenous protein with light-irradiation enhance bone repair via multiple osteogenic signal pathways, Biomaterials 284 (2022) 121482.
[57] W. Zhong, J. He, W. Huang, G. Yin, G. Liu, Y. Cao, J. Miao, Effect of the phosphorylation structure in casein phosphopeptides on the proliferation, differentiation, and mineralization of osteoblasts and its mechanism, Food Funct. 14 (2023) 10107–10118.
[58] T. Wang, J. Bai, M. Lu, C. Huang, D. Geng, G. Chen, L. Wang, J. Qi, W. Cui, L. Deng, Engineering immunomodulatory and osteoinductive implant surfaces via mussel adhesion-mediated ion coordination and molecular clicking, Nat. Commun. 13 (2022) 160.
[59] Q. Hu, Z. Tan, Y. Liu, J. Tao, Y. Cai, M. Zhang, H. Pan, X. Xu, R. Tang, Effect of crystallinity of calcium phosphate nanoparticles on adhesion, proliferation, and differentiation of bone marrow mesenchymal stem cells, J. Mater. Chem. 17 (2007) 4690–4698.
[60] X. Han, J. Shen, S. Chen, Z. Cai, Y. Zhu, W. Yi, K. Li, W. Cai, B. Tao, W. Cui, Ultrasonic-controlled "explosive" hydrogels to precisely regulate spatiotemporal osteoimmune disturbance, Biomaterials 295 (2023) 122057.